



UNIVERSITATEA DE MEDICINĂ ȘI FARMACIE  
„CAROL DAVILA”, BUCUREȘTI  
ȘCOALA DOCTORALĂ  
MEDICINĂ

TEZĂ DE DOCTORAT

Conducător de doctorat:  
Prof. Univ. Dr. Jinga Viorel

Student-doctorand:  
Bolocan Vlad-Octavian

2024



UNIVERSITATEA DE MEDICINĂ ȘI FARMACIE  
„CAROL DAVILA”, BUCUREȘTI  
ȘCOALA DOCTORALĂ  
MEDICINĂ

THE ROLE OF ARTIFICIAL INTELLIGENCE IN  
THE IDENTIFICATION OF RENAL ANATOMY  
AND CLEAR CELL RENAL CARCINOMA  
  
SUMMARY OF THE DOCTORAL THESIS

PhD Supervisor:  
Prof. Univ. Dr. Jinga Viorel

PhD Candidate:  
Bolocan Vlad-Octavian

2024

## Table of contents

<b>Fundamental Problem .....</b>	<b>2</b>
<b>Hypothesis .....</b>	<b>3</b>
<b>Objectives .....</b>	<b>3</b>
<b>Methodology .....</b>	<b>4</b>
<b>Study on Renal Anatomy Segmentation .....</b>	<b>5</b>
<b>Study on Segmentation and Classification of Clear Cell Renal Cell Carcinoma (ccRCC).....</b>	<b>6</b>
<b>Study on Adrenal Gland Segmentation .....</b>	<b>8</b>
<b>Conclusions and Personal Contributions.....</b>	<b>10</b>
<b>Selected bibliography .....</b>	<b>13</b>
<b>Appendices .....</b>	<b>18</b>

## List of Published Scientific Papers

1. **Bolocan V-O**, Secareanu M, Sava E, Medar C, Manolescu LSC, Cătălin Rașcu A-Ș, Costache MG, Radavoi GD, Dobran R-A, Jinga V. Convolutional Neural Network Model for Segmentation and Classification of Clear Cell Renal Cell Carcinoma Based on Multiphase CT Images. *Journal of Imaging*. 2023; 9(12):280. <https://doi.org/10.3390/jimaging9120280>
2. **Bolocan V-O**, Secareanu M, Sava E, Medar C, Manolescu LSC, Rașcu A-ȘC, Costache MG, Radavoi GD, Dobran R-A, Jinga V. Correction: Bolocan et al. Convolutional Neural Network Model for Segmentation and Classification of Clear Cell Renal Cell Carcinoma Based on Multiphase CT Images. *J. Imaging* 2023, 9, 280. *Journal of Imaging*. 2024; 10(2):35. <https://doi.org/10.3390/jimaging10020035>
3. **Bolocan V**, Diaconu G, Secareanu M, et al. (March 27, 2024) Renal Sinus Pathologies Depicted by CT Imaging: A Pictorial Review. *Cureus* 16(3): e57087. doi:10.7759/cureus.57087
4. **Bolocan V**, Diaconu G, Giuvelea A, et al. (July 31, 2024) Imaging Aspects in a Case of Persistent Müllerian Duct Syndrome (PMDS): A Case Report and Overview. *Cureus* 16(7): e65880. doi:10.7759/cureus.65880

## **Fundamental Problem**

The early and accurate diagnosis of renal tumors, particularly clear cell renal cell carcinoma, represents a major challenge in modern radiology. Since these tumors are often discovered at advanced stages, therapeutic options become limited, and patient prognosis significantly worsens. Kidney segmentation and the automatic classification of renal tumors are essential for improving early detection and optimizing clinical management. However, traditional imaging analysis methods face limitations related to the time required for manual interpretation, inter- and intra-observer variability, and reduced access to specialists in many medical institutions.

The development and implementation of automated solutions based on artificial intelligence (AI) offer a promising direction for overcoming these obstacles. Advanced deep learning algorithms have demonstrated the ability to analyze medical images with accuracy comparable to or even superior to human interpretation, enabling the automatic anatomical segmentation of the kidney and precise tumor classification. Their use could contribute to reducing diagnosis time and standardizing imaging assessments.

In Romania, the healthcare system faces specific challenges, including a shortage of specialized personnel, long waiting times for advanced investigations, and limited resources in regional hospitals. Therefore, integrating AI-based solutions could have a significant impact by optimizing the use of existing resources and improving patient access to a fast and accurate diagnosis. Internationally, numerous studies have demonstrated the efficiency of artificial intelligence technologies in medical imaging, but their practical implementation requires adaptation to the specificities of each healthcare system.

This research addresses this fundamental problem by exploring the potential of deep learning algorithms in kidney segmentation and renal tumor classification. The primary objective is to determine to what extent advanced convolutional neural network models can improve the accuracy and efficiency of imaging diagnosis, thereby contributing to the optimization of clinical workflow and enhancing the quality of medical care.

## **Hypothesis**

Advanced artificial intelligence models, particularly convolutional neural networks and deep learning architectures, have the potential to significantly improve the accuracy and efficiency of diagnosing clear cell renal carcinoma in medical imaging. It is hypothesized that the U-Net architecture, due to its encoder-decoder structure with skip connections, will provide more precise segmentation of renal tissues. Additionally, the ResNet101 model is expected to achieve a more accurate classification of normal and pathological renal tissues, surpassing the performance of other currently available models.

## **Objectives**

The objectives of this research focus on developing and validating AI-based solutions for kidney segmentation and renal tumor classification, aiming to enhance the accuracy and efficiency of imaging diagnosis.

A primary objective is to analyze the performance of convolutional neural network models in segmenting renal structures and identifying clear cell renal carcinoma. The study aims to evaluate various architectures to determine the most effective solutions capable of accurately differentiating normal from pathological structures.

In this context, the performance of U-Net, SegNet, and NablNet architectures will be compared concerning automatic kidney segmentation. A direct comparison of these models will be conducted using the Dice coefficient, a metric used to evaluate segmentation accuracy, to identify the algorithm that provides the most precise results.

The correct classification of renal tumors is another essential objective of the research, involving testing ResNet101 and ResNet152 architectures for characterizing images as normal or pathological. The study seeks to train and optimize these models to determine their applicability in diagnosing clear cell renal carcinoma.

To enhance model performance, another objective involves optimizing preprocessing and data augmentation techniques. The use of advanced methods such as rotation, mirroring, noise addition, and Gaussian filtering will contribute to improving model generalization and reducing the risk of overfitting.

Another important research direction is integrating these models into clinical practice, evaluating their impact on the workflow of radiologists. The study aims to

develop solutions that assist specialists in the faster and more precise diagnosis of renal tumors, thus facilitating timely access to appropriate treatment for patients.

To ensure the quality and accuracy of the data used in model training, the study also seeks to standardize the image preprocessing process. This includes detailed manual segmentation, conversion of images from DICOM format to formats compatible with machine learning models (NIFTI and PNG), and double validation of classifications by specialists. Creating an accurate and uniform dataset is essential for developing reliable and efficient models for the automatic diagnosis of clear cell renal carcinoma.

## **Methodology**

The overall methodology of this research is based on using the European Distributed Deep Learning (EDDLL) and European Computer Vision Library (ECVL) frameworks. These technologies are designed to integrate deep learning and advanced image processing into biomedical applications, facilitating the development of efficient models for medical image analysis.

EDDLL is an optimized library for distributed machine learning, capable of running efficiently on various hardware platforms, including CPUs, GPUs, and FPGAs. It enables the definition, training, and optimization of convolutional neural networks, offering flexibility in adapting algorithms to available resources. A major advantage of EDDLL is its ability to distribute training tasks across multiple computing units using pyCOMPSs, a programming model that optimizes the execution of neural networks on high-performance infrastructures.

ECVL plays a crucial role in data preprocessing and augmentation, facilitating the optimized handling of medical images for deep learning models. It allows the seamless integration of medical datasets and the application of advanced augmentation techniques, such as rotation, mirroring, noise addition, and Gaussian filtering, which are essential for improving model generalization and reducing overfitting.

Both libraries have been utilized for developing and testing AI models dedicated to kidney segmentation and renal tumor classification, enabling the efficient processing of large volumes of imaging data. Additionally, the EDDLL and ECVL infrastructures have been optimized for high-performance hardware execution, reducing model training time and facilitating their integration into clinical practice.

## Study on Renal Anatomy Segmentation

This study aimed to evaluate the use of machine learning techniques for renal anatomy segmentation, focusing on the convolutional neural network (CNN) architectures U-Net, SegNet, and NablNet. Precise segmentation is essential for the early diagnosis and effective treatment of renal diseases, making the identification of the most efficient model a key objective.

The methodology involved a cohort of 913 patients, with 457 having a healthy right kidney and 456 having a healthy left kidney. The cases were selected from the database of the "Professor Doctor Theodor Burghel" Clinical Hospital in Bucharest between 2015 and 2019, with the inclusion criterion being the absence of significant imaging alterations in the kidneys. The image preprocessing steps included anonymization, normalization, and data augmentation through rotations, Poisson noise, Gamma correction, and Gaussian filtering. The models tested were U-Net, SegNet, and NablNet, with their performance assessed using the Dice coefficient and key performance indicators such as time-to-model-in-production (TTMP), time-of-training-models (TOTM), and time-of-pre-processing-images (TOPPI).

The study results indicated that U-Net had the best performance, achieving a Dice score of 0.81, while NablNet reached 0.43, and SegNet recorded the weakest performance with a score of only 0.025. In terms of computational efficiency, the time required for implementing the U-Net model in production was 3.821 minutes for right kidney segmentation and 4.052 minutes for the left kidney. Regarding model training, the time per epoch was 38.19 minutes for the right kidney and 40.5 minutes for the left kidney. The preprocessing stage took 20 minutes per dataset, in addition to a fixed time of 12.5 hours required for the development of the YML tool.

Comparing the results with existing literature, it was observed that more advanced architectures, such as U-Net enhanced with attention mechanisms or EfficientNet, achieved higher Dice scores, ranging between 0.83 and 0.96. Additionally, SegNet exhibited poor performance in other studies as well, consistently being outperformed by modern architectures such as nnU-Net. Regarding training time, the values obtained in this study were competitive compared to other research, but models incorporating attention mechanisms or dense architectures demonstrated superior performance.

The conclusions of this study highlight that U-Net is the most effective architecture among those tested, offering an optimal balance between precision and computational efficiency. On the other hand, SegNet proved to be ineffective for kidney segmentation, struggling to retain fine image details. To enhance segmentation performance, future research should explore the integration of attention mechanisms, optimization of preprocessing methods, and the development of multimodal architectures. This study demonstrates the applicability of machine learning in kidney segmentation and underscores the need for more accurate and resilient models.

## **Study on Segmentation and Classification of Clear Cell Renal Cell Carcinoma (ccRCC)**

The primary objective of this study was to evaluate the application of machine learning algorithms for the segmentation and classification of clear cell renal cell carcinoma (ccRCC). The importance of this research lies in the necessity for a rapid and precise diagnosis of this pathology, which directly impacts therapeutic decisions and patient prognosis. The study focused on testing and comparing the architectures ResNet101 and ResNet152 to determine the optimal method for tumor segmentation and classification.

The study was conducted retrospectively on a cohort of 160 patients selected from the database of the "Professor Doctor Theodor Burghele" Clinical Hospital in Bucharest between 2016 and 2019. Among these patients, 76 had renal involvement on the right side, while 84 had involvement on the left side. The inclusion criteria targeted patients with a histopathologically confirmed diagnosis of conventional renal carcinoma who underwent multiphase CT scans before any surgical interventions or therapeutic procedures. Conversely, patients with other types of renal neoplasms or with imaging artifacts that hindered detailed analysis were excluded.

Data preprocessing was a crucial phase of the study and included image anonymization, normalization, augmentation through techniques such as rotations, Poisson noise addition, gamma correction, Gaussian filtering, and manual segmentation of regions of interest. The processed data were used to train and validate convolutional neural network models.

For the classification of normal and pathological kidneys, the study tested the ResNet101 and ResNet152 models. ResNet101, with a depth of 101 layers, demonstrated superior performance compared to ResNet152, achieving an accuracy of 85%, compared to 71% for the latter model. This difference led to the decision to continue training and further testing exclusively with the ResNet101 architecture.

Model performance evaluation was based on several key performance indicators. One such indicator, "time-to-diagnose," showed a significant reduction in the time required for a physician to diagnose a patient, from 420 seconds to just 12 seconds per patient, through the integration of the machine learning model. Another metric, "time-to-study-a-population," demonstrated that the duration required to analyze a large dataset of medical images decreased from 1057 minutes to 30.2 minutes, facilitating the rapid assessment of large patient populations.

Another essential aspect analyzed was "time-to-model-in-production," which measures the duration of model deployment in a production environment. The study demonstrated a substantial improvement in this parameter, reducing the implementation time to 190 minutes for the right kidney and 189 minutes for the left kidney, down from initial values of 397 and 601 minutes, respectively.

Regarding "time-of-training-models," a significant optimization was achieved, with values of 2.63 minutes per epoch for the right kidney and 4 minutes per epoch for the left kidney in the intermediate phase, further reduced to 1.26 minutes per epoch for the right kidney and 1.25 minutes per epoch for the left kidney in the final phase. These values are competitive compared to similar studies, highlighting the efficiency of implementing ResNet101 in the classification process.

The quality of tumor segmentation was measured using the Dice coefficient, which reached values of 0.71 for the right kidney and 0.64 for the left kidney, indicating good performance but with potential for improvement. In terms of classification, the final accuracy was 0.92 for the right kidney and 0.85 for the left kidney, demonstrating the high precision of the ResNet101 model in diagnosing renal tumors.

Comparing the results with previous studies revealed that the obtained values for accuracy and efficiency were competitive or even superior to those reported in earlier research using similar models. Studies that applied ResNet101 in other fields of medical imaging, such as deep vein thrombosis classification or Alzheimer's disease detection, reported accuracies ranging from 0.87 to 0.98, suggesting that ResNet101 could be further optimized to enhance ccRCC classification.

In conclusion, this study demonstrated that the use of machine learning models, particularly ResNet101, can significantly reduce the time required for diagnosis and population-level analysis while maintaining high classification accuracy. Implementing such a model in clinical practice could provide substantial benefits, enabling rapid and precise renal cancer diagnosis. Future research should focus on further optimizing the model by incorporating attention mechanisms and advanced data augmentation strategies to enhance segmentation and classification accuracy.

## **Study on Adrenal Gland Segmentation**

The primary objective of this study was to develop and evaluate deep learning models for the automatic segmentation of the adrenal glands, which are small structures with a complex anatomical location. Accurate segmentation of the adrenal glands is essential for diagnosing and monitoring endocrine disorders and adrenal tumors. The integration of artificial intelligence (AI) models can significantly enhance the accuracy and efficiency of these processes.

To achieve this goal, the study tested and compared three convolutional neural network (CNN) architectures—U-Net, SegNet, and NablaNet—to determine the most effective model for adrenal gland segmentation. Several key performance indicators were analyzed, including the time required to implement the model in a clinical setting ("Time-of-Model-in-Production" – TTMIP), the time needed to train the models ("Time-of-Training-Models" – TOTM), and the time necessary for image preprocessing ("Time-of-Pre-Processing-Images" – TOPPI). The segmentation performance was assessed using the Dice coefficient, a standard metric that measures the overlap between automated and manually created segmentations.

The dataset used consisted of 3D CT images collected under standardized conditions, including 435 cases for the right adrenal gland and 433 cases for the left adrenal gland. To ensure data validity and quality, strict inclusion criteria were established, including image clarity and adherence to a complete CT protocol. Exclusion criteria focused on eliminating scans with major artifacts or incomplete data. The processing and training of models were conducted on a high-performance system featuring an Nvidia GeForce RTX 2080 Ti GPU and the Ubuntu 20.04.4 LTS operating system.

Among the three architectures tested, U-Net demonstrated the best results, achieving a Dice coefficient of 0.63 for the right adrenal gland and 0.66 for the left adrenal gland. Although these values fell short of the predicted level of 0.8, they were significantly better than those obtained by SegNet (0.30) and NablaNet (0.55). The superior performance of U-Net can be attributed to its skip connection-based architecture, which preserves fine details and critical spatial relationships essential for segmenting small structures. SegNet struggled to retain the fine details necessary for precise segmentation, while NablaNet, despite being more computationally efficient, failed to outperform U-Net.

Regarding production implementation time (TTMIP), the U-Net model demonstrated rapid integration, with an average time of 1 minute for the right adrenal gland and 1.2 minutes for the left adrenal gland. This confirms the feasibility of using this model in clinical practice, with a highly competitive transition time compared to similar models in the literature.

Model training duration (TOTM) ranged between 6.63 and 8.1 minutes per epoch, indicating a high level of efficiency in deep learning processes. Compared to other studies reporting training times of 10-15 minutes per epoch for similar models, these results suggest good computational resource optimization. Additionally, the time required for image preprocessing (TOPPI) was approximately 20 minutes per dataset, with an additional fixed time of 12.5 hours dedicated to the development and configuration of the YML tool. This duration aligns with other studies in the field, where extensive medical image preprocessing can take between 20 and 30 minutes per dataset.

Comparing these results with the existing literature highlighted both the strengths and limitations of the study. For instance, a study by Rajamani et al. reported a Dice coefficient of 87.2% for automatic adrenal gland segmentation using models optimized with attention mechanisms, suggesting that integrating such mechanisms could significantly improve segmentation performance. Conversely, other studies have shown that models like SegNet struggle to retain fine details, confirming the findings of this study regarding the limitations of this architecture.

In conclusion, this study demonstrated that deep learning models can be used for automatic adrenal gland segmentation, but their accuracy remains below the optimal level required for widespread clinical application. The U-Net model provided the best results but requires further improvements to achieve the desired accuracy. Enhancing image preprocessing, utilizing more advanced architectures, and integrating attention

mechanisms could improve performance. Moreover, diversifying the dataset and testing advanced data augmentation strategies could reduce result variability and enhance model generalization.

In the long term, the effective implementation of automatic adrenal gland segmentation in clinical practice will require refining existing architectures and adopting hybrid solutions that combine the strengths of multiple models. This study provides a solid foundation for future research, highlighting both the potential and challenges associated with using deep learning for adrenal gland segmentation.

## **Conclusions and Personal Contributions**

The proposed objectives of this research were largely achieved, covering the segmentation of normal kidneys, the classification of clear cell renal cell carcinoma (ccRCC), and an attempt to segment the adrenal glands using similar methods. Segmentation was performed using the U-Net architecture, which demonstrated high efficiency, achieving a Dice score of 0.81. This performance is comparable to the standards reported in the literature and underscores the model's ability to accurately delineate the complex anatomical contours of the kidneys. Minor differences between this study and others in the literature can be attributed to variations in datasets used, model optimizations, and the quality of available medical images.

The high accuracy of segmentation is clinically relevant, directly impacting patient diagnosis and monitoring. The U-Net model demonstrated a robust ability to identify essential anatomical structures, facilitating medical analysis and reducing the time required for manual image processing. While some studies have achieved slightly higher scores by using architectures with attention mechanisms or DenseNet, U-Net remains a balanced solution, combining computational efficiency with high accuracy.

For the classification of ccRCC, the ResNet101 model delivered notable results, achieving an accuracy of 0.92 for the right kidney and 0.85 for the left kidney. These values surpass many similar studies, where accuracy typically ranges between 0.75 and 0.85. The superior performance of ResNet101 can be attributed to its use of residual blocks, which maintain an optimal flow of information and facilitate the learning of complex medical imaging features. Additionally, the application of advanced data

augmentation techniques increased dataset variability, preventing overfitting and improving the model's ability to generalize to other image sets.

The results indicate that CNNs can significantly contribute to optimizing clinical processes. The models developed in this study significantly reduced the time required for diagnosis and population analysis. The average time for establishing a diagnosis decreased from 420 seconds per patient to just 12 seconds, marking a substantial improvement in clinical efficiency. Furthermore, the time required to analyze an extensive dataset, relevant for epidemiological studies and therapeutic decision-making, was reduced from 1057 minutes to 30.2 minutes. These optimizations facilitate the management of large data volumes and allow physicians to focus more on interpreting results and making therapeutic decisions.

From an economic perspective, implementing AI technologies in medical imaging involves substantial initial investments, particularly in hardware infrastructure and IT system adaptation. However, the long-term benefits are evident, reducing costs associated with manual data processing, improving diagnostic accuracy, and minimizing medical errors. In healthcare systems like Romania's, where resources are often limited, adopting such solutions could optimize the use of equipment and personnel, contributing to better organization of medical activities and increased patient access to rapid and precise investigations.

Despite these advances, some unresolved challenges remain. Adrenal gland segmentation did not achieve the expected performance, with a maximum Dice score of 0.66, indicating the need for model improvements. A potential solution could involve integrating attention mechanisms to capture fine anatomical details more effectively. Additionally, optimizing training and production times is a critical research direction, as reducing computational resource demands would facilitate the large-scale implementation of these solutions in clinical practice.

The personal contributions to this study focused on optimizing and implementing the two fundamental models used: U-Net for kidney and adrenal gland segmentation and ResNet101 for ccRCC classification. A major contribution was adapting the U-Net model to the specific dataset by adjusting hyperparameters and implementing advanced data augmentation techniques. These modifications enabled the achievement of a competitive Dice score of 0.81 for the kidneys, consistent with the latest studies in the field. For adrenal glands, the results were more modest; however, comparative analysis identified clear

directions for performance improvement, such as using hybrid architectures or attention mechanisms.

For ccRCC classification, a significant contribution was the implementation and optimization of the ResNet101 model, which outperformed other tested architectures. The optimization of residual block structures allowed the model to learn relevant features more effectively without encountering gradient vanishing issues. Additionally, integrating advanced data augmentation techniques increased dataset variability and improved model generalization.

A key aspect of this research was the significant reduction in diagnostic and analysis time. The reduction of diagnostic time from 420 seconds to 12 seconds per patient had a major impact on clinical workflow efficiency, enabling physicians to quickly access essential information for therapeutic decisions. Moreover, the time required for analyzing an extensive patient population was significantly reduced, allowing for rapid and efficient epidemiological assessments.

In conclusion, this research confirms that machine learning models for kidney segmentation and tumor classification can significantly enhance diagnostic accuracy and efficiency. While the results are promising, especially for kidneys, adrenal gland segmentation remains a challenge, and future studies should explore advanced solutions such as attention mechanisms or multimodal architectures. Further optimization is needed to balance model performance with computational efficiency for seamless clinical integration.

## Selected bibliography

1. Hosny A, Parmar C, Quackenbush J, Schwartz LH, Aerts HJWL. Artificial intelligence in radiology. *Nat Rev Cancer* 2018;18:500–10.
2. Mazurowski MA, Buda M, Saha A, Bashir MR. Deep learning in radiology: An overview of the concepts and a survey of the state of the art with focus on MRI. *Journal of Magnetic Resonance Imaging* 2019;49:939–54.
3. Gallée L, Kniesel H, Ropinski T, Götz M. Artificial intelligence in radiology – beyond the black box. *RöFo - Fortschritte auf dem Gebiet der Röntgenstrahlen und der bildgebenden Verfahren* 2023;195:797–803.
4. Petch J, Di S, Nelson W. Opening the Black Box: The Promise and Limitations of Explainable Machine Learning in Cardiology. *Canadian Journal of Cardiology* 2022;38:204–13.
5. Kharat AT, Singhal S. A peek into the future of radiology using big data applications. *Indian J Radiol Imaging* 2017;27:241–8.
6. Pisano ED, Garnett LR. Big Data and Radiology Research. *Journal of the American College of Radiology* 2019;16:1347–50.
7. Kansagra AP, Yu JPJ, Chatterjee AR, Lenchik L, Chow DS, Prater AB, et al. Big Data and the Future of Radiology Informatics. *Acad Radiol* 2016;23:30–42.
8. Krizhevsky A, Sutskever I, Hinton GE. ImageNet classification with deep convolutional neural networks. *Commun ACM* 2017;60:84–90.
9. Simonyan K, Zisserman A. Very Deep Convolutional Networks for Large-Scale Image Recognition. 2014;
10. Yasaka K, Abe O. Deep learning and artificial intelligence in radiology: Current applications and future directions. *PLoS Med* 2018;15:e1002707.
11. Ronneberger O, Fischer P, Brox T. U-Net: Convolutional Networks for Biomedical Image Segmentation. Olaf Ronneberger, Philipp Fischer, Thomas Brox 2015;
12. Shin HC, Roth HR, Gao M, Lu L, Xu Z, Nogues I, et al. Deep Convolutional Neural Networks for Computer-Aided Detection: CNN Architectures, Dataset Characteristics and Transfer Learning. *IEEE Trans Med Imaging* 2016;35:1285–98.
13. What is Overfitting?
14. Tajbakhsh N, Shin JY, Gurudu SR, Hurst RT, Kendall CB, Gotway MB, et al. Convolutional Neural Networks for Medical Image Analysis: Full Training or Fine Tuning? *IEEE Trans Med Imaging* 2016;35:1299–312.
15. Zeiler MD, Fergus R. Visualizing and Understanding Convolutional Networks. 2014. page 818–33.
16. Lin S-Y, Lin C-L. Brain tumor segmentation using U-Net in conjunction with EfficientNet. *PeerJ Comput Sci.* 2024;10:e1754.
17. Cheng D, Gai J, Mao Y, Gao X, Zhang B, Jing W, et al. EA-Net: Research on skin lesion segmentation method based on U-Net. *Heliyon.* 2023;9:e22663.

18. Yousef R, Khan S, Gupta G, Albahlal BM, Alajlan SA, Ali A. Bridged-U-Net-ASPP-EVO and Deep Learning Optimization for Brain Tumor Segmentation. *Diagnostics*. 2023;13:2633.
19. Su F, Zhang W, Liu Y, Chen S, Lin M, Feng M, et al. The development and validation of pathological sections based U-Net deep learning segmentation model for the detection of esophageal mucosa and squamous cell neoplasm. *J Gastrointest Oncol*. 2023;14:1982–92.
20. van der Schot A, Sikkel E, Niekolaas M, Spaanderman M, de Jong G. Placental Vessel Segmentation Using Pix2pix Compared to U-Net. *J Imaging*. 2023;9:226.
21. Fu L, Li S. A New Semantic Segmentation Framework Based on UNet. *Sensors*. 2023;23:8123.
22. Peng Y, Xu Y, Wang M, Zhang H, Xie J. The nnU-Net based method for automatic segmenting fetal brain tissues. *Health Inf Sci Syst*. 2023;11:17.
23. Yadav N, Dass R, Virmani J. Objective assessment of segmentation models for thyroid ultrasound images. *J Ultrasound*. 2022;26:673–85.
24. Khalal DM, Azizi H, Maalej N. Automatic segmentation of kidneys in computed tomography images using U-Net. *Cancer/Radiothérapie*. 2023;27:109–14.
25. Khanna A, Londhe ND, Gupta S. A Deep Attention-based U-Net for Airways Segmentation in Computed Tomography Images. *Curr Med Imaging Rev*. 2023;19.
26. Guo X, Xiao R, Lu Y, Chen C, Yan F, Zhou K, et al. Cerebrovascular segmentation from TOF-MRA based on multiple-U-net with focal loss function. *Comput Methods Programs Biomed*. 2021;202:105998.
27. Müller D, Kramer F. MIScnn: a framework for medical image segmentation with convolutional neural networks and deep learning. *BMC Med Imaging*. 2021;21:12.
28. Wang Y, Guo Y, Wang Z, Yu L, Yan Y, Gu Z. Enhancing semantic segmentation in chest X-ray images through image preprocessing: ps-KDE for pixel-wise substitution by kernel density estimation. *PLoS One*. 2024;19:e0299623.
29. Nazir I, Haq IU, Khan MM, Qureshi MB, Ullah H, Butt S. Efficient Pre-Processing and Segmentation for Lung Cancer Detection Using Fused CT Images. *Electronics (Basel)*. 2021;11:34.
30. Fakhouri HN, Alawadi S, Awaysheh FM, Alkhabbas F, Zraqou J. A cognitive deep learning approach for medical image processing. *Sci Rep*. 2024;14:4539.
31. Okada T, Linguraru MG, Hori M, Summers RM, Tomiyama N, Sato Y. Abdominal multi-organ segmentation from CT images using conditional shape–location and unsupervised intensity priors. *Med Image Anal*. 2015;26:1–18.
32. Korfiatis P, Denic A, Edwards ME, Gregory A V., Wright DE, Mullan A, et al. Automated Segmentation of Kidney Cortex and Medulla in CT Images: A Multisite Evaluation Study. *Journal of the American Society of Nephrology*. 2022;33:420–30.
33. Gibson E, Giganti F, Hu Y, Bonmati E, Bandula S, Gurusamy K, et al. Automatic Multi-Organ Segmentation on Abdominal CT With Dense V-Networks. *IEEE Trans Med Imaging*. 2018;37:1822–34.
34. Li D, Xiao C, Liu Y, Chen Z, Hassan H, Su L, et al. Deep Segmentation Networks for Segmenting Kidneys and Detecting Kidney Stones in Unenhanced Abdominal CT Images. *Diagnostics*. 2022;12:1788.

35. Salvadori J, Allegrini O, Opsommer T, Carullo J, Sarrut D, Porot C, et al. Anatomy-based correction of kidney PVE on  $^{177}\text{Lu}$  SPECT images. *EJNMMI Phys.* 2024;11:15.
36. Linguraru MG, Pura JA, Pamulapati V, Summers RM. Statistical 4D graphs for multi-organ abdominal segmentation from multiphase CT. *Med Image Anal.* 2012;16:904–14.
37. Chu C, Oda M, Kitasaka T, Misawa K, Fujiwara M, Hayashi Y, et al. Multi-organ Segmentation Based on Spatially-Divided Probabilistic Atlas from 3D Abdominal CT Images. 2013. p. 165–72.
38. Okada T, Linguraru MG, Hori M, Summers RM, Tomiyama N, Sato Y. Abdominal Multi-organ CT Segmentation Using Organ Correlation Graph and Prediction-Based Shape and Location Priors. 2013. p. 275–82.
39. Wu J, Kamath M V., Noseworthy MD, Boylan C, Poehlman S. Segmentation of Images of Abdominal Organs. *Crit Rev Biomed Eng.* 2008;36:305–34.
40. Nakayama Y, Sato M, Okamoto M, Kondo Y, Tamura M, Minagawa Y, et al. Deep learning-based classification of adequate sonographic images for self-diagnosing deep vein thrombosis. *PLoS One.* 2023;18:e0282747.
41. Zheng Y, Deng L, Lin Q, Xu W, Wang F, Li J. KRS-Net: A Classification Approach Based on Deep Learning for Koi with High Similarity. *Biology (Basel).* 2022;11:1727.
42. Thirumalaisamy S, Thangavilou K, Rajadurai H, Saidani O, Alturki N, Mathivanan S kumar, et al. Breast Cancer Classification Using Synthesized Deep Learning Model with Metaheuristic Optimization Algorithm. *Diagnostics.* 2023;13:2925.
43. Zahid U, Ashraf I, Khan MA, Alhaisoni M, Yahya KM, Hussein HS, et al. BrainNet: Optimal Deep Learning Feature Fusion for Brain Tumor Classification. *Comput Intell Neurosci.* 2022;2022:1–13.
44. Alquran H, Al-Issa Y, Alsalatie M, Mustafa WA, Qasmieh IA, Zyout A. Intelligent Diagnosis and Classification of Keratitis. *Diagnostics.* 2022;12:1344.
45. You Z, Han B, Shi Z, Zhao M, Du S, Yan J, et al. Vocal cord leukoplakia classification using deep learning models in white light and narrow band imaging endoscopy images. *Head Neck.* 2023;45:3129–45.
46. Mukhtorov D, Rakhmonova M, Muksimova S, Cho Y-I. Endoscopic Image Classification Based on Explainable Deep Learning. *Sensors.* 2023;23:3176.
47. Li H, Chen Y, Wang Q, Gong X, Lei Y, Tian J, et al. Convolutional neural network-based automatic cervical vertebral maturation classification method. *Dentomaxillofacial Radiology.* 2022;51.
48. Sun X, Zhang L, Luo Q, Zhou Y, Du J, Fu D, et al. Application of Machine Learning in the Diagnosis of Early Gastric Cancer Using the Kyoto Classification Score and Clinical Features Collected from Medical Consultations. *Bioengineering.* 2024;11:973.
49. Jain R, Singh P, Abdelkader M, Boulila W. Efficient lung cancer detection using computational intelligence and ensemble learning. *PLoS One.* 2024;19:e0310882.
50. Mirbabaie M, Stieglitz S, Frick NRJ. Artificial intelligence in disease diagnostics: A critical review and classification on the current state of research guiding future direction. *Health Technol (Berl).* 2021;11:693–731.

51. Richens JG, Lee CM, Johri S. Improving the accuracy of medical diagnosis with causal machine learning. *Nat Commun.* 2020;11:3923.
52. Zhang X, Wang X, Xu L, Liu J, Ren P, Wu H. The predictive value of machine learning for mortality risk in patients with acute coronary syndromes: a systematic review and meta-analysis. *Eur J Med Res.* 2023;28:451.
53. Amador S, Beuschlein F, Chauhan V, Favier J, Gil D, Greenwood P, et al. Deep Learning Approaches Applied to Image Classification of Renal Tumors: A Systematic Review. *Archives of Computational Methods in Engineering.* 2024;31:615–22.
54. Badawy M, Almars AM, Balaha HM, Shehata M, Qaraad M, Elhosseini M. A two-stage renal disease classification based on transfer learning with hyperparameters optimization. *Front Med (Lausanne).* 2023;10.
55. Zhao T, Sun Z, Guo Y, Sun Y, Zhang Y, Wang X. Automatic renal mass segmentation and classification on CT images based on 3D U-Net and ResNet algorithms. *Front Oncol.* 2023;13.
56. Sabharwal Y. NephroNet: A Novel Program for Identifying Renal Cell Carcinoma and Generating Synthetic Training Images with Convolutional Neural Networks and Diffusion Models. 2023;
57. Abdelrahman A, Viriri S. FPN-SE-ResNet Model for Accurate Diagnosis of Kidney Tumors Using CT Images. *Applied Sciences.* 2023;13:9802.
58. Chanchal AK, N S, Lal S, Kumar S, Saxena PP. Classification and grade prediction of kidney cancer histological images using deep learning. *Multimed Tools Appl.* 2024;83:78247–67.
59. Zhang M, Ye Z, Yuan E, Lv X, Zhang Y, Tan Y, et al. Imaging-based deep learning in kidney diseases: recent progress and future prospects. *Insights Imaging.* 2024;15:50.
60. Türk F, Lüy M, Barışçı N. Kidney and Renal Tumor Segmentation Using a Hybrid V-Net-Based Model. *Mathematics.* 2020;8:1772.
61. Sun P, Mo Z, Hu F, Song X, Mo T, Yu B, et al. 2.5D MFFAU-Net: a convolutional neural network for kidney segmentation. *BMC Med Inform Decis Mak.* 2023;23:92.
62. Kittipongdaja P, Siriborvornratanakul T. Automatic kidney segmentation using 2.5D ResUNet and 2.5D DenseUNet for malignant potential analysis in complex renal cyst based on CT images. *EURASIP J Image Video Process.* 2022;2022:5.
63. Li F, Yang M, Li Y, Zhang M, Wang W, Yuan D, et al. An improved clear cell renal cell carcinoma stage prediction model based on gene sets. *BMC Bioinformatics.* 2020;21:232.
64. Jagga Z, Gupta D. Classification models for clear cell renal carcinoma stage progression, based on tumor RNAseq expression trained supervised machine learning algorithms. *BMC Proc.* 2014;8:S2.
65. Tian K, Rubadue CA, Lin DI, Veta M, Pyle ME, Irshad H, et al. Automated clear cell renal carcinoma grade classification with prognostic significance. *PLoS One.* 2019;14:e0222641.
66. Alhussaini AJ, Steele JD, Jawli A, Nabi G. Radiomics Machine Learning Analysis of Clear Cell Renal Cell Carcinoma for Tumour Grade Prediction Based on Intra-Tumoural Sub-Region Heterogeneity. *Cancers (Basel).* 2024;16:1454.

67. Bektas CT, Kocak B, Yardimci AH, Turkcanoglu MH, Yucetas U, Koca SB, et al. Clear Cell Renal Cell Carcinoma: Machine Learning-Based Quantitative Computed Tomography Texture Analysis for Prediction of Fuhrman Nuclear Grade. *Eur Radiol.* 2019;29:1153–63.
68. Rajamani KT, Rani P, Siebert H, ElagiriRamalingam R, Heinrich MP. Attention-augmented U-Net (AA-U-Net) for semantic segmentation. *Signal Image Video Process.* 2023;17(4):981-989. doi: 10.1007/s11760-022-02302-3. Epub 2022 Jul 25. PMID: 35910403; PMCID: PMC9311338.
69. Bhalodiya JM, Lim Choi Keung SN, Arvanitis TN. Magnetic resonance image-based brain tumour segmentation methods: A systematic review. *Digit Health.* 2022 Mar 16;8:20552076221074122. doi: 10.1177/20552076221074122. PMID: 35340900; PMCID: PMC8943308.
70. Barstuğan M, Ceylan R, Asoglu S, Cebeci H, Koplay M. Adrenal tumor segmentation method for MR images. *Comput Methods Programs Biomed.* 2018 Oct;164:87-100. doi: 10.1016/j.cmpb.2018.07.009. Epub 2018 Jul 18. PMID: 30195434.

## **Appendices**

## Appendix 1



Journal of  
*Imaging*



Article

---

### Convolutional Neural Network Model for Segmentation and Classification of Clear Cell Renal Cell Carcinoma Based on Multiphase CT Images

---

Vlad-Octavian Bolocan, Mihaela Secareanu, Elena Sava, Cosmin Medar,  
Loredana Sabina Cornelia Manolescu, Alexandru-Ștefan Cătălin Rașcu, Maria  
Glencora Costache,  
George Daniel Radavoi, Robert-Andrei Dobran and Viorel Jinga



Journal of  
*Imaging*



Article

### Convolutional Neural Network Model for Segmentation and Classification of Clear Cell Renal Cell Carcinoma Based on Multiphase CT Images

Vlad-Octavian Bolocan <sup>1,2</sup>, Mihaela Secareanu <sup>2</sup>, Elena Sava <sup>2</sup>, Cosmin Medar  
<sup>1,2</sup>, Loredana Sabina Cornelia Manolescu <sup>1,\*</sup>, Alexandru-Ștefan Cătălin  
Rașcu <sup>3,4</sup>, Maria Glencora Costache <sup>1</sup>, George Daniel Radavoi <sup>3,4</sup>, Robert-  
Andrei Dobran <sup>5</sup> and Viorel Jinga <sup>3,4,6</sup>



**Citation:** Bolocan, V.-O.; Secareanu,

---

#### <sup>1</sup>. Introduction

Renal cell carcinomas are a group of malignant tumors originating from epithelial cells lining the renal tubules that are divided into multiple histological subtypes. The most common is the clear cell type (70–90%), followed by papillary (10–15%) and chromophobe (3–5%). Other subtypes are collecting duct carcinoma, MiT family translocation renal cell carcinomas, tubulocystic carcinomas, etc. [1].

M.; Sava, E.; MDPI, Basel, Switzerland. This article is an open access article  
Medar, C.; distributed under the terms and conditions of the Creative  
Manolescu, Commons Attribution (CC BY) license ([https://  
L.S.C.; Cațălin creativecommons.org/licenses/by/  
Ras, cu, A.-S. ; 4.0/](https://creativecommons.org/licenses/by/4.0/)).

Costache, <sup>1</sup> Department of Fundamental Sciences, Faculty of Midwifery  
M.G.; Radavoi, and Nursing, University of Medicine and Pharmacy “Carol  
G.D.; Dobran, R.- Davila”, 050474 Bucharest, Romania; vlad-  
A.; Jinga, V. octavian.bolocan@drd.umfcd.ro (V.-O.B.);  
Convolutional cosmin.medar@umfcd.ro (C.M.); maria.costache@umfcd.ro  
Neural (M.G.C.)

Network Model for <sup>2</sup> Department of Clinical Laboratory of Radiology and  
Segmentation and Medical Imaging, Clinical Hospital “Prof. Dr. Theodor  
Classification of Burghele”, 050664 Bucharest, Romania;  
Clear Cell Renal mihaela.secareanu@rez.umfcd.ro (M.S.);  
Cell elena.sava@rez.umfcd.ro (E.S.)

Carcinoma Based <sup>3</sup> Department of Urology, Clinical Hospital “Prof. Dr.  
on Multiphase CT Theodor Burghele”, Faculty of Medicine, University of  
Images. *J. Imaging* Medicine and Pharmacy “Carol Davila”, 050474 Bucharest,  
**2023**, 9, 280. Romania; stefan.rascu@umfcd.ro (A.-S. .C.R.);  
[\[jimaging9120280\]\(https://doi.org/10.3 jimaging9120280\) <sup>4</sup> Department of Urology, Clinical Hospital “Prof. Dr.  
Received: 6 Theodor Burghele”, 050664 Bucharest, Romania](https://doi.org/10.3 daniel.radavoi@umfcd.ro (G.D.R.); viorel.jinga@umfcd.ro<br/>390/ (V.J.)</a></p></div><div data-bbox=)

November 2023 <sup>5</sup> Software Imagination & Vision (Simavi), 013685  
Revised: 8 Bucharest, Romania; robert.dobran@simavi.ro

December 2023 <sup>6</sup> Medical Sciences Section, Academy of Romanian  
Accepted: 12 Scientists, 050085 Bucharest, Romania

December 2023 \* Correspondence: loredana.manolescu@umfcd.ro

Published: 14 **Abstract:** (1) Background: Computed tomography (CT) imaging  
December 2023 challenges in diagnosing renal cell carcinoma (RCC) include  
Corrected: 29 distinguishing malignant from benign tissues and determining the  
January 2024 likely subtype. The goal is to show the algorithm’s ability to  
improve renal cell carcinoma identification and treatment,



**Copyright:** © (2) Methods: This study uses the  
2023 by the European Deep-Health toolkit’s Convolutional Neural Network  
authors. Licensee with ECVL, (European Computer Vision Library), and EDDL,

(European Distributed Deep Learning Library). Image segmentation utilized U-net architecture and resnet101. The model's clinical efficiency was assessed utilizing kidney, tumor, Dice score, and renal cell carcinoma categorization quality. (3) Results: The raw dataset contains 457 healthy right kidneys, 456 healthy left kidneys, 76 pathological right kidneys, and 84 pathological left kidneys. Preparing raw data for analysis was crucial to algorithm implementation. Kidney segmentation performance was 0.84, and tumor segmentation mean

Dice score was 0.675 for the suggested model. Renal cell carcinoma classification was 0.885 accurate. (4) Conclusion and key findings: The present study focused on analyzing data from both healthy patients and diseased renal patients, with a particular emphasis on data processing. The method achieved a kidney segmentation accuracy of 0.84 and mean Dice scores of 0.675 for tumor segmentation. The system performed well in classifying renal cell carcinoma, achieving an accuracy of 0.885, results which indicates that the technique has the potential to improve the diagnosis of kidney pathology.

**Keywords:** convolutional neural network; renal cell carcinoma; image segmentation; image classification; artificial intelligence; kidney tumor; European Deep Health toolkit; EDDL; ECVL

Among all urogenital types of cancer, renal cell carcinomas are the most prevalent. These malignancies were the sixth most frequently diagnosed cancers in men and the tenth most common cancers diagnosed in women worldwide [2,3]. The majority of renal cell carcinomas are diagnosed incidentally due to the increased availability and usage of imaging modalities, which resulted in a decreasing trend in tumor size and stage [4]. The size and presence of local invasion are key features in the staging and treatment options for renal cell carcinoma (RCC) tumors. When possible, it is desirable to preserve as many nephrons as possible using kidney-sparing surgery for tumor removal. In these cases, cancer recurrence affects 20–40% of patients with localized RCC [5].

Multiphase contrast-enhanced computed tomography (CT) is strongly recommended for diagnosing and staging RCC. Other complementary imaging techniques are magnetic resonance imaging (MRI) and contrast-enhanced ultrasound [6]. Sensitivity for the detection of renal masses using CT is at about 87%, and even higher for lesions greater than 2 cm. Additionally, the specificity in the case of these tumors is 74.5% [7]. The challenging aspects of diagnosing RCC on CT imaging are differentiating malignant tissues from benign tissues (especially clear cell carcinoma versus oncocytoma or fat-free angiomyolipoma), as well as assessing the probable subtype of RCC [8].

It is important to note that this paper brings together the fields of radiology and computer science. Therefore, in order to increase the readability and clarify of the findings, we have added the following list as succinct definitions for key terms we have used:

**AI (Artificial Intelligence):** AI refers to the development of computer systems that can perform tasks that typically require human intelligence, such as problem solving, learning, and decision making.

**Machine Learning:** Machine learning is a subset of AI that involves the use of algorithms and statistical models to enable computers to improve their performance on a task without explicit programming, relying on patterns and inference instead.

**Convolutional Neural Network (CNN):** A type of neural network designed for visual processing, CNNs use convolutional layers to

automatically and adaptively learn hierarchical features from data, making them effective for image recognition tasks.

**U-net Model:** The U-net model is a specific architecture in deep learning, particularly used for image segmentation tasks. It is characterized by a U-shaped architecture, which allows effective feature extraction and segmentation.

**RasNet101 Model:** RasNet101, or ResNet101, is a specific convolutional neural network

(CNN) architecture renowned for its depth, featuring 101 layers. Widely used in image recognition tasks, ResNet architectures, including ResNet101, leverage residual learning to effectively train deep neural network.

**EDDL (Embedded Deep Learning):** EDDL involves integrating deep learning capabilities into embedded systems, enabling them to perform complex tasks locally without relying on external computing resources.

**ECVL (Embedded Computer Vision Library):** ECVL refers to a library designed for embedded systems, focusing on computer vision tasks. It aids in implementing computer vision algorithms efficiently on devices with limited computational resources.

Due to recent developments, artificial intelligence now offers an unprecedented opportunity to harness large amounts of data and sophisticated algorithms. It has also been adopted in the medical field, and especially in the radiology domain, as a useful tool for physicians to make more accurate diagnoses and classifications in significantly lower time [9,10]. Whilst the field of artificial intelligence is very wide and there are several artificial intelligence algorithms available, convolutional neural networks (CNNs)—a subclass of deep learning algorithms—have emerged as the most popular modality for processing images [11]. In a survey conducted by Geert Litjens et al. [10], CNNs have been found to be the most preferred approach for medical image interpretation, turning them into current standard practice.

From a hierarchical point of view, deep learning is a subtype of machine learning, which is, in turn, a subclass of artificial intelligence. Deep learning differentiates itself from other machine learning subtypes through the ability of the algorithm to learn, on its own, which features are best for a given computational task, compared to the case in which a human expert chooses certain imaging features that appear to best

represent the visual data [12]. Neural networks, the foundation of deep learning algorithms, sometimes known as artificial neural networks (ANNs) or simulated neural networks (SNNs), are used for this purpose. They are known as “neural” because they resemble the way the brain neurons communicate with one another.

Neural networks are made up of three main layers—an input layer, a hidden layer

(which may comprise several layers), and an output layer (Figure 1). Each node, which links to the next node as an artificial neuron, has a weight and a threshold value. One node is activated and begins sending data to the following layer of the network when its output exceeds the threshold value. When it falls below the threshold, no data are sent. While the input and output layers are always fixed, the hidden layers vary in number, size, and specialization, depending on the type of network.

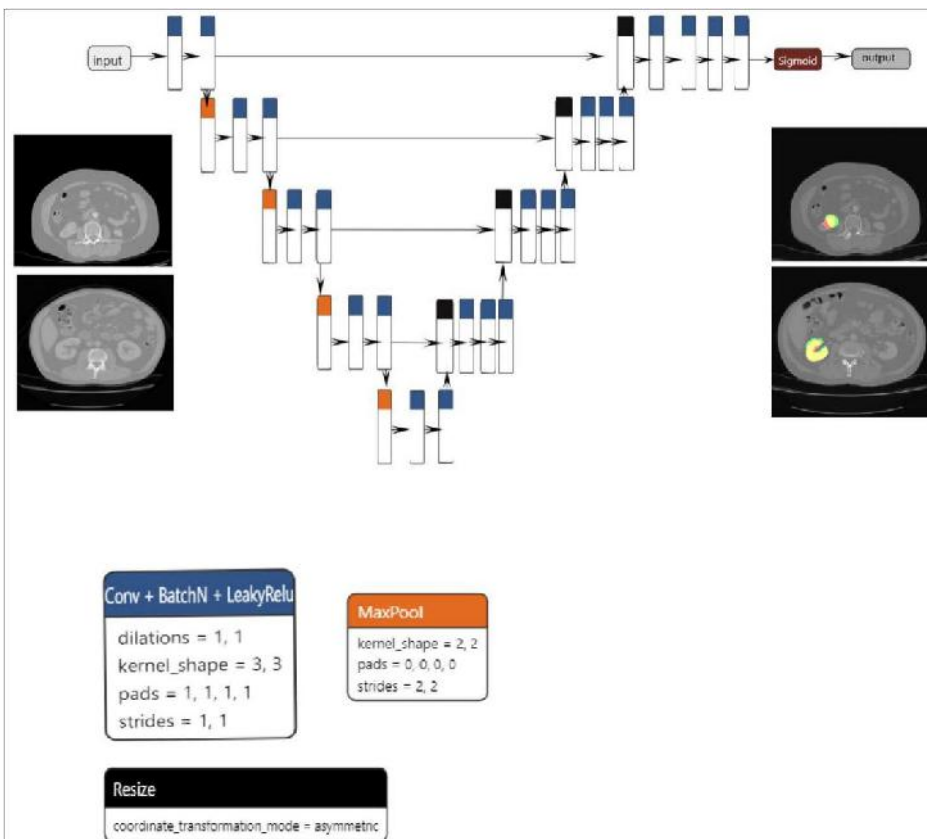


**Figure 1.** U-net model used.

The primary hidden types of layers combined to build a CNN are the convolutional layer, the pooling layer, and the fully connected layer [13]. The convolutional and the pooling layers act as feature extractors from the base image, while the fully connected layer acts as a classifier.

These layers are interconnected in intricate ways, making it challenging to interpret exactly how the network transforms the input into the final output. As a result, it becomes difficult to comprehend which specific features or patterns the CNN focuses on during its analysis, giving CNNs the alias of “black boxes”, due to their underlying complexity [14]. CNNs could extract tangled features from medical images by employing multiple hidden layers of artificial neurons, mimicking the intricate processing of the human visual cortex, with each layer performing specific operations on the input data.

The main areas where CNNs have proven their value in the radiology field are related to object detection, segmentation, and classification [12]. Object detection refers to the ability of the algorithm to determine the presence of objects, as well as their precise location. In medical imaging, it can be used to identify organs, lesions, or tumors. However, the output is represented as a box containing the desired object, as well as other nearby structures. In order to demarcate the exact item though, a segmentation algorithm must be used, as it involves identifying and outlining specific structures or areas of interest within an image, and enables precise measurements, quantification, and analysis of specific regions or abnormalities. Finally, image classification involves categorizing images into predefined classes or categories, distinguishing between different diseases or pathologies based on the visual characteristics present in the image, for example, classifying a CT scan slice as benign or malignant based on the presence of tumor.

The primary metrics for assessing how well the algorithm performs are the Dice score and the Accuracy index [15]. The Dice score is often used to evaluate how well the algorithm can accurately outline or segment an object by measuring the overlap between its predicted segmentation and the actual (ground truth) segmentation. On the other hand, Accuracy is employed to gauge how accurately the algorithm classifies or categorizes different elements.

The significance of the tumor segmentation task is evident via the establishment of the Kidney and Kidney Tumor Segmentation Challenge [16], a competitive event designed to identify the most effective system for the automated semantic segmentation of kidneys and renal tumors. The competition was conducted in the years 2019 and 2021, and the present event is the 2023 iteration. The authors of the

study, Zhongchen Zhao et al. [17], were the winners of the 2021 Kidney and Renal Tumor Segmentation Challenge. In their research, they utilized a U-net convolutional neural network (CNN) to perform the segmentation of both the kidney and renal masses. The obtained results showed average Dice scores of 0.908 and 0.860 for the segmentation of the kidney and kidney masses, respectively. Jianhui Wen et al. [18] introduced a squeeze-and-excitation encoder–decoder network called SeResUNet, which bears resemblance to the U-net design. The authors reported somewhat lower Dice scores of 0.672 and 0.545 for the kidney segmentation task and renal tumor segmentation, respectively.

Zheng Gong et al. [19] created a neural network model based on SCNet that can do two things at once: segmenting and classifying kidney tumors. The model achieved a Dice score of 0.846 for tumor segmentation and an accuracy metric of 0.995 for classifying malignant tumors. For sorting kidney tumors into different groups, Alzu’bi et al. [20] suggested making a two-dimensional convolutional neural network with four layers, which they called CNN-4. This model achieved a notable accuracy rate of 92% in effectively discerning between benign and malignant tumors.

Within the framework of this paper, our main aim is to thoroughly assess the effectiveness of a convolutional neural network (CNN) method. This assessment includes two crucial components, segmentation and classification, as they both play a significant role in the diagnosis and management of renal cell carcinoma (RCC). The incorporation of convolutional neural networks (CNNs) in this domain signifies a noteworthy progression in the discipline. Our research strives to conduct a thorough evaluation of the efficacy of CNNs in precisely segmenting and categorizing cases of renal cell carcinoma (RCC). Through the utilization of these performance indicators, our objective is to elucidate the algorithm’s capacities and its potential to augment the diagnosis and treatment of RCC, thereby making a valuable contribution to the enhancement of patient care and outcomes.

## **2. Materials and Methods**

The CNN employed in this project is the one developed as part of the European DeepHealth toolkit [21], an open-source framework whose aim is to boost biomedical applications by using cutting-edge deep learning and computer vision algorithms.

The DeepHealth toolkit comprises two integrated software libraries: ECVL (European Computer Vision Library) and EDDL (European Distributed Deep Learning Library), which were created expressly for computer vision and deep learning tasks [22–24].

EDDL is a general-purpose deep learning library initially developed to address deep learning requirements in healthcare use cases within the DeepHealth project, and supports widely used deep neural network topologies, including convolutional and sequence-to-sequence models. However, as CNNs have been found to be highly effective [11], with high selectivity and invariance, they are also the most common DNN used for biomedical images. The main layers of CNN are the input layer, convolutional layer, pooling layer, fully connected layers, and the output layer (Figure 1).

The proposed segmentation model, which is based on the U-net architecture, consists of three blocks: convolution, encoding, and decoding. The convolution, encoding, and decoding phases are implemented using convolutional layers, with a stride of one and a total of 23 convolutional layers in the architecture. Following the application of each convolutional layer, batch normalization and LeakyRelu activation are performed. In order to reduce spatial dimensions, the convolutional layers on the encoder block are linked together via max pooling layers.

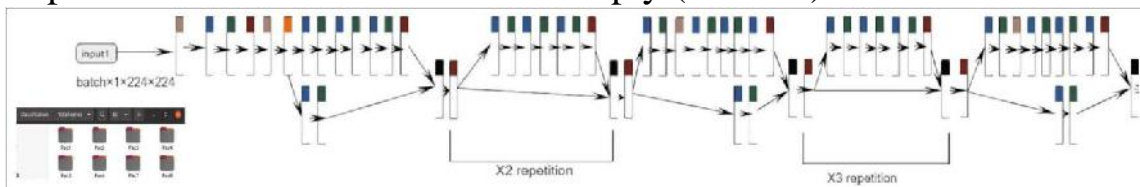
The decoder block concatenates the resized tensor with the skip connection tensor that was generated by the encoder block that corresponds to it. A sigmoid activation function is subsequently implemented on the output tensor. The dimensions of both the input and output are  $1 \times 224 \times 224$ . Data augmentation techniques, including elastic transform, color transformation, grid distortion, and image rotation, were applied to both the training and validation sets in order to mitigate the risk of overfitting. The Adam optimizer was utilized to optimize the model.

The primary benefit of the convolutional layer is that it only considers a neuron's immediate surroundings, and that all neurons inside a layer share the same weights. This significantly decreases the number of parameters and, hence, the memory space needed to store a layer of this type. Additionally, pooling is an operation that is used to reduce the

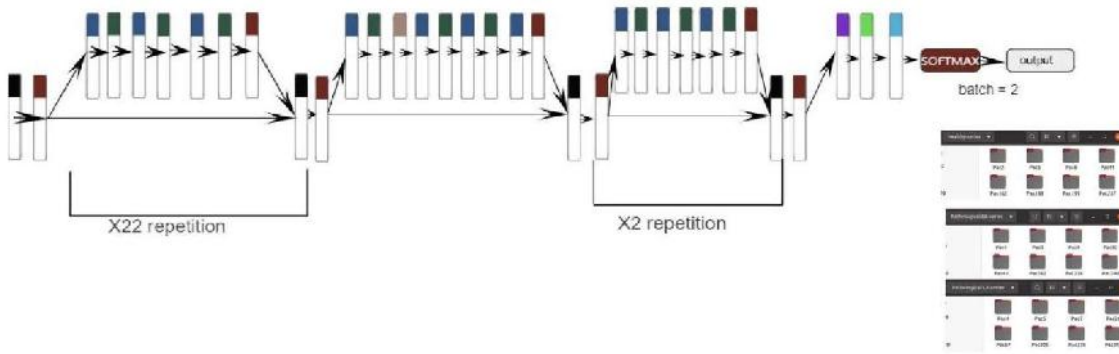
scale of the input. Pooling takes subsamples of the convolutional layer to feed the next layer, acting as a powerful detector of patterns independently of their relative position in the image. Weight sharing in convolutional layers combined with pooling schemes (max or average pooling) allows the extraction of position-invariant relevant properties. For the current project, the main use case was image classification and segmentation in the process of diagnosing renal tumors. As a result, three main tasks were defined: kidney segmentation, tumor segmentation, and tumor classification.

Regarding medical image segmentation tasks, well-known architectures that are supported by the EDDL library are U-net and V-net. U-net was first introduced in 2015 and has shown very good performance on very different biomedical segmentation applications [25] and was the architecture used for both kidney and tumor segmentation tasks.

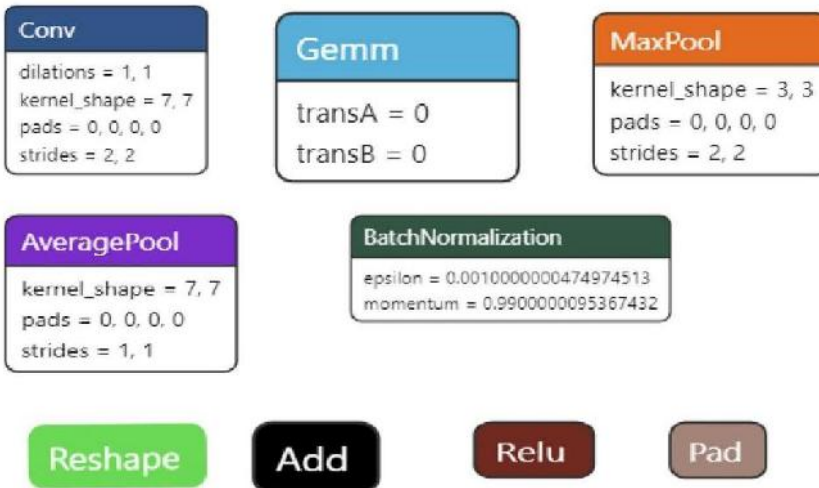
For the classification task, the model used was based on the resnet101 architecture (Figure 2a–c), which, as the name suggests, has 101 layers and can classify up to 1000 classes. However, for this paper, we restricted the use to up to two classes. The classification model is built upon the ResNet101 architecture, which includes 33 residual blocks and a total of 104 convolutional layers. The first layer has a kernel size of  $7 \times 7$  and a stride of 2, while the subsequent levels have kernel sizes of  $1 \times 1$  and  $3 \times 3$ , all with a stride of 1. Each convolutional layer is followed by a batch normalization step. To ensure the initial collection of the most significant features, the network employs max pooling at an early stage. Conversely, average pooling is employed towards the end to accentuate the overall content of the feature maps. The network utilizes the Relu activation function throughout all layers, although in the final step of the architecture, the softmax function is applied. The final layer of the network employs a matrix multiplication operation, specifically implemented as General Matrix Multiply (GEMM).



(a)



(b)



(c)

**Figure 2.** (a)—ResNet101 part 1. (b)—ResNet101 part 2. (c)—ResNet101 part 3.

ECVL is designed to serve two main purposes, allowing an easy integration and data exchange between existing libraries, including EDDL, and the availability of performance testing frameworks, which will allow repeatable experiments on large scale datasets to verify the impact of different modifications.

The image class represents the core of the entire ECVL library. It is an object that stores data (either images/videos or raw data) in a multi-dimensional dense numerical single or multi-channel tensor. The tensor is a vector or matrix used in machine learning for storing data. The ECVL library supports all common data formats, as well as NIfTI and DICOM, providing both reading, writing, and most of the image manipulation and processing functionalities. Furthermore, a visualizer for 3D volumes, such as CT scans, allows one to observe different slices of a volume from different views.

Data partitioning is a key step for training neural networks. The split process is performed via ECVL in order to provide EDDL with the required data for training and validation steps. The data augmentation process allows the artificial enlargement of a dataset by perturbing the training data in realistic ways, mimicking variability between different CT scanners or image acquisition timing to prevent overfitting and thus improving the training process of neural networks and increasing the final accuracy. Overfitting is an undesirable machine learning behavior that occurs when the machine learning model gives accurate predictions for training data but not for test data [26]. The ECVL library includes all the augmentation strategies commonly exploited in the literature, such as flipping, adding salt-and-pepper noise, blurring an image, or adjusting the contrast [27].

The cooperation between EDDL and ECVL was achieved by defining the DeepHealth Dataset Format (DDF), which is based on the YAML syntax. The YAML is a data serialization language mainly used for writing configuration files. Serialization is a process where one application or service that has different data structures and is written in a different set of technologies, and can transfer data to another application using a standard format. This format defines all the information such as the name and description of the dataset, its classes and features, a list of image or volume paths, and a split indicating how to divide images into training, validation, and test sets. The DeepHealth Dataset Format also allows the specification of segmentation masks for each input entry. An ECVL module is provided to parse and load DDF defined datasets into the specific dataset class. The library's interface is based on two main functions that convert ECVL Image(s) into EDDL Tensor(s) and vice versa.

The dataset provided was used both for training the model in kidney segmentation and RCC classification and for performing inferences. The raw dataset consisted of DICOM images corresponding to four-phase contrast-enhanced CT (pre-contrast, arterial, venous, and excretory phase). For this project, only arterial phase images were used. After installing and configuring all necessary tools, the data have been anonymized and annotated. In the case of segmentation, a segmentation of the area of interest was performed, which was then saved in NIfTI format. For the classification task, each patient was labeled with or

without a tumor. Then, the relevant series were extracted from the raw DICOM data. Using a tool to create YMLs and selecting the required parameters, the data were transformed into DeepHealth Dataset Format. Afterwards, the model was trained on this dataset; inferences were performed in order to determine whether the resulting model was suitable; the final step was validating the results.

These steps were performed for both the segmentation and classification of the right and left kidney, separately. Tumor segmentation was executed on the right and left kidney.

We used the following parameters for segmentation and classification, Table 1.

**Table 1.** Parameters.

<b>Segmentation</b>	<b>Classification</b>
Learning rate: 0.0001	Learning rate: 0.0001
Epochs: 100	Epochs: 100
Batch size: 8	Batch size: 20
Loss: DICE	Loss Binary Cross Entropy
Metric: DICE	Metric: accuracy
Height: 224	Height: 224
Width: 224	Width: 224

The number of batches between synchronizations of weights is a crucial configuration parameter to achieve speedups close to the optimum. This parameter is dynamically adjusted to bound the communications overhead to be lower than the percentage given as a reference. Another important parameter is the batch size. While all the tensors necessary to conduct all the computations of the train batch operation fit in the memory of the GPU, larger batch sizes allow the EDDL to better leverage the full potential of GPUs.

The raw dataset consisted of 457 kidneys from patients with a healthy right kidney, 456 kidneys from patients with a healthy left kidney, 76 kidneys from patients with a pathological right kidney, and 84 kidneys from patients who had a pathological left kidney, Tables 2 and 3.

**Table 2.** Raw dataset of healthy kidneys.

<b>Dataset</b>	<b>Number of Patients</b>	<b>Size of Original Data (GB)</b>	<b>Size of Processed Data (GB)</b>	<b>Size of Segmentation (GB)</b>	<b>Number of Images</b>
Healthy right kidney	457	345.5	59.22	62.3	119,853
Healthy left kidney	456	344.5	59.22	62.2	119,529

**Table 3.**

Raw dataset of pathological kidneys.

<b>Dataset</b>	<b>Number of Patients</b>	<b>Size of Original Data (GB)</b>	<b>Size of Processed Data (GB)</b>	<b>Size of Segmentation (GB)</b>	<b>Number of Images</b>
Pathological right kidney	76	31.65	7.48	7.43	13,248
Pathological left kidney	84	35.93	8.76	9.32	18,133

The training process begins with an input YAML file, which serves as a mapping tool. This YAML file specifies how to handle the dataset, DICOM data, and NIfTI data, especially in cases involving segmentations. On the other side of the training pipeline, the output is comprised of two primary components: a trained model saved in the ONNX format, which is specifically designed for representing machine learning models, and a collection of PNG images.

These PNG images are generated based on the initial DICOM data and serve different purposes depending on the type of training being performed. For segmentation tasks, some PNG images display the results of the model’s predictions, showcasing the regions it has identified, while others show the ground truth masks for comparison. In classification tasks, the PNG images are organized into separate folders based on the predicted classes assigned by the model. This output structure helps to assess the performance and effectiveness of the trained model. Some of the factors relevant in deciding whether the model is suitable or not are key performance indicators (KPIs), as seen in Table 4. KPIs are data points and measurement tools that can be used to

monitor and evaluate the quality of services provided by a radiology operation [28].

**Table 4.** The main KPIs that were calculated throughout the entire project.

---

measures how much time it takes a medical

Time-to-diagnose professional to diagnose urology problems for one patient

---

measures the time necessary to complete an entire training session with sufficient epochs to assure

convergence to the desired performance on the test set

Time-to-model-in-production ttmip

(epochs defines the number times that the learning algorithm will work through the entire training dataset)

---

Time-of-training-models totm	measures the execution time of the training process per epoch
Time-of-pre-processing-images toppi	measures the time necessary to accomplish all the preprocessing tasks (installing software, anonymizing and annotating data, etc.)
Kidney segmentation quality	measures how well the model predicts the region of interest using the DICE score as indicator
Tumor segmentation quality	measures how well the model predicts the region of interest using the DICE score as indicator
Classification quality of renal cell carcinoma (RCC)	The metric used for this KPI is accuracy

---

Apart from the time-to-model-in-production, time-of-training-models, and time-ofpre-processing-images KPIs (considering that these time-consuming tasks have to be carried out only once at the beginning of the project), all the other indicators can and will be used in this paper to assess the efficiency of the CNN model in clinical practice.

The study was peer-validated and approved by the Ethics Committee of the “Profesor Dr. Th. Burghele” Clinical Hospital, Bucharest, Romania (approval number 2/2021), and all procedures in the study respected the ethical standards of the Helsinki Declaration. Informed consent was obtained from all participants.

### 3. Results

#### 3.1. Model Comparison

U-net was chosen above SegNet and NablaNet for segmentation, Tables 5 and 6. Before library training, datasets were augmented. At the time the SegNet libraries did not handle DICOM data; therefore, we transformed DICOM and NIFTI data to PNG, which was unsatisfactory. The neural network training of the NablaNet model using only NIFTI data did not enhance Dice scores. Our U-net model yielded the best results, achieving a Dice score of up to 0.81. We used ResNet101 and ResNet152 for the classification task and found that ResNet101 worked best.

**Table 5.** Segmentation model comparison.

<b>Model</b>	<b>Dice Score Value</b>
SegNet	0.025
NablaNet	0.43
U-net	0.81

**Table 6.** Classification model comparison.

<b>Model</b>	<b>Accuracy Value</b>	<b>Score</b>
ResNet152	0.71	
ResNet101	0.82	

The following tables further illustrate the comparison with other models, i.e., ResNet101, that we have tested before settling on U-net.

#### 3.2. Pre-Processing

The pre-processing of data, as seen in Table 7, consisted mainly of time series epoching/ segmentation, filtering, artefact detection/rejection; the areas of interest were highlighted and the radiological description was added. Anonymization steps were first performed. Afterwards, depending on the case (segmentation vs. classification task), a segmentation of the area of interest is performed, or each patient was

labelled as having a tumor or not. Afterwards, the relevant series containing the needed information from each patient were extracted.

The time to run each step was as follows:

- 5 min/patient to anonymize;
- 12 min/patient to perform the segmentation;
- 1 min/patient series extraction time;
- 12 h to develop and 30 min to install the YML tool based on DICOM and NIFTI data; This was carried out only once and does not depend on the task or the organ;
- 2 min/patient to run the pipeline time.

**Table 7.** Pre-processing of data.

Task	Organ	Anonymization + Segmentation Time	Total Time in Intermediate Stage	Total Time in Final Stage
Time of pre-processing images	Right kidney	17 min/patient	20 min/patient + 12.5 h fixed time	20 min/patient + 12.5 h fixed time
	Left kidney	17 min/patient	20 min/patient + 12.5 h fixed time	20 min/patient + 12.5 h fixed time
Segmentation				
Classification	Right kidney	5 min/patient	5 min/patient + 12.5 h fixed time	5 min/patient + 12.5 h fixed time

---

Left kidney	5 min/patient	5 min/patient + 12.5 h fixed time	5 min/patient + 12.5 h fixed time
-------------	---------------	-----------------------------------	-----------------------------------

---

### 3.3. KPIs Results

As stated in Section 2, the main KPIs used to assess the efficiency of the model in clinical practice are time-to-diagnose, kidney segmentation quality, tumor segmentation quality, and classification quality of renal cell carcinoma (RCC). In the following sections, all these KPIs are addressed.

#### 3.3.1. Kidney and Tumor Segmentation Quality

Kidney segmentation quality measures how well the model predicts the zone of interest using the Dice score as indicator, as seen in Table 8. This Dice coefficient measures the overlap between the two NIfTI masks: first the original segmentation mask with the kidney and the second mask is the one predicted by the model. The target Dice score for the project was 0.8. The results are presented in Table 8.

**Table 8.** Results of kidney and tumor segmentation quality.

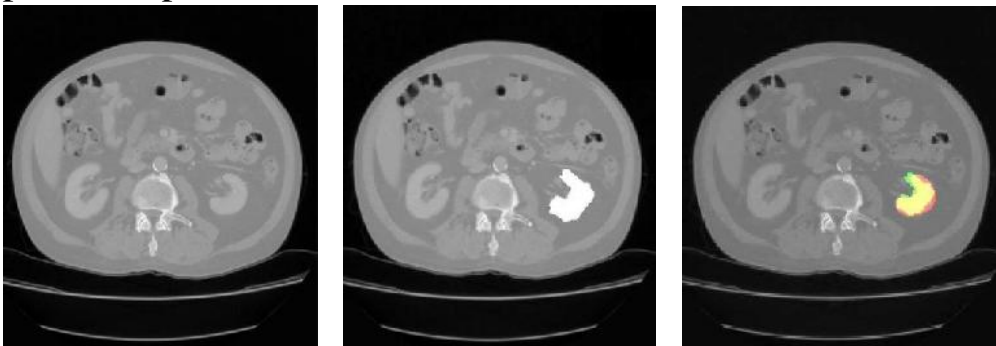
---

Task	Organ	Expected Target at the End of the Project	Intermediate Stage	Final Stage
Kidney segmentation quality (Dice score)	Right kidney	0.80	0.81	0.84
	Left kidney	0.80	0.80	0.84
Segmentation Pathological quality (dice score)	Pathological right kidney	0.80	0.73	0.71
	Pathological left kidney	0.80	0.73	0.64

---

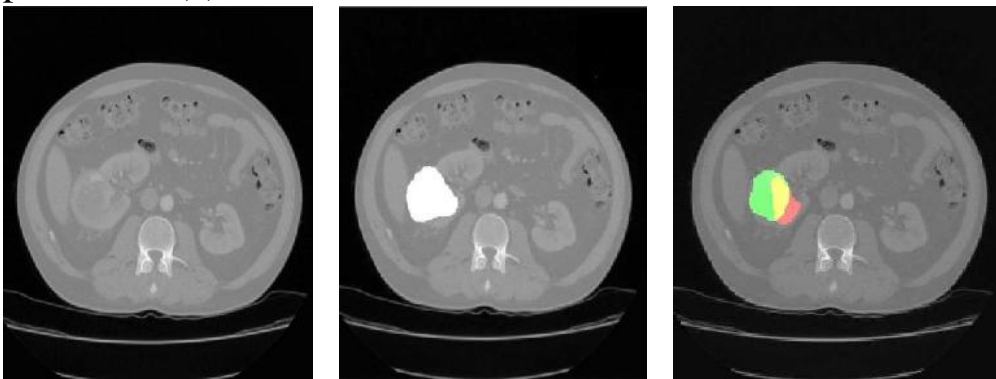
The comparison of the output results of the segmentation network and the expert segmentation of a healthy kidney is shown in Figure 3, while for the pathological kidney (renal tumor), the comparison of the output

results of the segmentation network and the expert segmentation of a healthy kidney is shown in Figure 4. Regarding the potential bias of the medical experts, although it cannot be eliminated, we have striven to greatly reduce this bias by triple checking the segmentation of the area of interest. Therefore, a radiology resident (V.O.B.), a radiology fellow (G.M.C.), and a radiology attending physician (C.M.), with a combined 25 years of experience imaging renal cell carcinoma, utilized 3D Slicer [29] to manually segment the dataset. Concerning the color scheme utilized below, the red area represents the prediction, the green area the ground truth. The yellow area, therefore, represents the correctly predicted pixels.



(a) (b) (c)

**Figure 3.** CT image of a healthy kidney (a); the medical expert segmentation (shown in white) (b); and the result of the model's prediction (c).



(a) (b) (c)

**Figure 4.** CT image of a kidney with clear cell renal cell carcinoma (a); the medical expert tumor segmentation (shown in white) (b); and the result of the tumor location prediction (c).

### 3.3.2. Classification Quality of Clear Renal Cell Carcinoma (cRCC)

The dataset is classified by the trained model in one of two classes: patient with normal kidney or patient with tumor, Table 9. The validity

of the model was assessed by using the accuracy metric. The patient was diagnosed based on the number of images belonging to them that were classified as healthy or containing a tumor. The overall score was calculated based on how many patients were diagnosed correctly.

**Table 9.** Dataset for classification quality of clear renal cell carcinoma.

Task	Organ	Expected Target at the End of the Project	Intermediate of Stage	Final Stage
Classification quality of clear renal cell carcinoma for patients	Right of kidney	0.70	0.94	0.92
	Left kidney	0.70	0.85	0.85

Classification (accuracy)

The complete dataset was split into 70-20-10 training, validation, and test datasets

(occasionally 70-10-20). Validation and metric calculation followed each epoch (dice for segmentation, accuracy for classification). If the metric for that epoch exceeded the best prior one, an ONNX model was recorded. Finally, the model from the epoch with the best validation dataset performance was used. Testing this ONNX model on the test dataset was the second stage. A C++ inference source code file was created to display the prediction on the test dataset and compute the ONNX model's performance. A C++ source code file that displays the projection but does not compare it to the ground truth was also created. Segmentation and classification validation and testing differ. Each image's Dice metric is calculated during validation and testing for segmentation. Image measurements are averaged to determine the total metric. Two categorization methods are utilized. In the first method, accuracy is calculated for each image and averaged throughout the validation or test dataset. The total measure shows how successfully the model diagnosed each image. In the second technique, accuracy metrics

are determined for each image and a patient’s diagnosis is based on whether more of their images are healthy or not. How many cases were accurately diagnosed determines the final score.

To prevent overfitting, the dataset was split into three: training, validation, and testing. Even if the process ran for 100 epochs, only trained models that performed well on the validation dataset (that was not used in the training proper) were considered. Further testing was conducted on the test dataset to check whether the trained model could perform on other input data. Thus, the method of early stopping was used to prevent overfitting. Additionally, a diverse and large dataset was also used to prevent overfitting, as well as data augmentation. We implemented various data augmentation techniques in our model to mitigate the risk of overfitting. These techniques included resizing to dims with cubic interpolation, conversion to 32-bit float, mirroring with probability, rotation by angle, addition of Poisson noise, Gamma contrast, Gaussian blur, and Coarse dropout.

### 3.3.3. Time-to-Diagnose

The time-to-diagnose KPI measures how much time it takes to diagnose a renal clear cell carcinoma for a given patient, Table 10. The baseline value indicates the time that a diagnosis of a clear renal cell carcinoma would take without using machine learning tools, while the final stage indicates the time to diagnose the tumor using the libraries and the trained model.

**Table 10.** Time-to-diagnose KPI.

	<b>Baseline Stage</b>	<b>Final Stage</b>
Time-to-diagnose	420 s/patient	12 s/patient

## 4. Discussion

In this study, the data preprocessing was of the uttermost importance, as it prepared the input for the subsequent analysis. The process encompassed several essential procedures, namely time series epoching/segmentation, filtering, artifact detection/rejection, and the subsequent identification of regions of interest, which were then subjected to radiological description. The first stage included in the process was anonymization, which aimed to safeguard patient privacy and ensure the security of the data. Various methods were conducted depending on the specific goal at hand, such as segmentation or classification. In the context of segmentation tasks, the region of interest

underwent a process of segmentation, whereas in classification tasks, patients were assigned labels indicating the presence or absence of a tumor. Following this, pertinent data sets comprising crucial patient information were extracted. The average duration of the anonymization method each patient was 5 min, while the segmentation technique took around 12 min per patient. Additionally, the series extraction procedure required approximately 1 min per patient. In addition, the YML tool was developed and implemented using DICOM and NIfTI data, requiring a total of 12 h. It is important to note that this was a singular undertaking and not contingent on the particular activity or organ involved. Ultimately, the execution of the pipeline for each individual patient necessitated a time commitment of 2 min. The preprocessing stages established the groundwork for the later evaluation of key performance indicators (KPIs).

The assessment of the model's effectiveness in clinical practice involved the consideration of various key performance indicators (KPIs), as detailed in Section 2. The key performance indicators (KPIs) encompassed in this study are time-to-diagnose, kidney segmentation quality, tumor segmentation quality, and classification quality of renal cell carcinoma (RCC). A thorough analysis was conducted on each of these key performance indicators (KPIs) to gain a comprehensive understanding of the model's performance.

A score called the Dice score was used to check the quality of the kidney segmentation. This score measures how much the predicted segmentation mask made by the model and the original segmentation mask for the kidney overlap. A benchmark Dice score of 0.8 was set as the aim for the project, representing the ideal level of accuracy in kidney segmentation. The evaluation of the classification accuracy of clear renal cell carcinoma (cRCC) was conducted by assessing the model's capacity to correctly categorize patients into two categories: those with a healthy kidney and those with a tumor. The metric employed to assess the validity of the model was accuracy. The diagnosis of patients was determined by assessing the number of images identified as either healthy or containing a tumor. Subsequently, an overall accuracy score was computed to evaluate the correctness of patient diagnoses.

The accurate segmentation of tumors holds a critical position in the diagnostic and therapeutic processes related to clear cell renal cell

carcinoma (cRCC). The precise delineation of the tumor mass is crucial for effective surgical planning, especially in cases where partial nephrectomy is considered. Partial nephrectomy involves the selective removal of only the malignant tissue, preserving the surrounding healthy kidney tissue. Therefore, it becomes paramount to accurately identify and outline the tumor boundaries in relation to the renal collective system for optimal medical decision-making.

The model we have suggested demonstrated a segmentation performance of 0.84 for the task of kidney segmentation, accompanied by a mean Dice score of 0.675 for tumor segmentation. The aforementioned values exhibit a slight decrease in comparison to the results reported by Zhongchen Zhao et al. [17], which were 0.908 and 0.860, respectively. In contrast, the Dice scores for both kidney segmentation and kidney mass segmentation, which were 0.84 and 0.675, respectively, exhibited superior performance compared to the metrics provided by Jianhui Wen et al. [18]. Their scores were 0.672 for kidney segmentation and 0.545 for kidney mass segmentation.

Our model achieved a segmentation performance score of 0.675 for renal masses, which was a little lower than the 0.846 score reported by Zheng Gong et al. [19]. However, it is important to note that the accuracy measure was more consistent across the studies. Our model demonstrated an accuracy score of 0.885, whereas Zheng Gong et al. reported an accuracy measure of 0.995. Additionally, there was a slighter difference in the accuracy measure when compared to the model that Dalia Alzu'bi et al. [20] suggested. Their model achieved an accuracy rate of 0.92, whereas our model earned a score of 0.885.

The metric known as “time-to-diagnose” functioned as a crucial key performance indicator (KPI) that measured the duration necessary to diagnose renal clear cell carcinoma in individual patients. The baseline value denoted the duration required for tumor diagnosis without the utilization of machine learning techniques, whereas the final stage indicated the time taken to diagnose the tumor with the aid of libraries and the trained model. The key performance indicators (KPIs) in question offer a comprehensive evaluation of the model’s performance within the context of clinical practice. They provide insights into the model’s efficiency and efficacy in facilitating the diagnosis of renal cell carcinoma.

### *Limitations of the Study*

The findings of this study necessitate careful consideration within the scope of certain limitations. Firstly, the size of our patient cohort, in contrast to the datasets commonly available for artificial intelligence (AI) segmentation challenges, was comparatively smaller. This limitation stemmed from the labor-intensive nature of manual data preprocessing, impacting the breadth and diversity of the dataset. Consequently, the accuracy of our model may be tempered when benchmarked against what might have been achievable with a more extensive and diverse dataset. This constraint highlights the intrinsic tradeoff between dataset size and the rigor of manual preprocessing, influencing the model's performance metrics.

Secondly, the constrained dataset introduces the potential for overfitting, particularly attributable to the inclusion of skip connections and additional layers in the expanding path. These architectural choices resulted in a notable escalation in the number of parameters, potentially making the model more prone to fitting noise in the training data rather than capturing essential patterns. The interplay between dataset limitations and model complexity underscores the delicate balance required in designing neural network architectures for optimal performance.

Furthermore, our study explored specific segmentation and classification architectures, namely U-net, SegNet, NablNet, ResNet101, and ResNet152. While U-net demonstrated superior performance among the segmentation models and ResNet101 and ResNet152 were the sole models considered for classification, other architectures such as EfficientNet for segmentation and V-Net and SCNet for both tasks could have yielded promising results. However, due to resource constraints and an extended testing period, our study was circumscribed in its exploration of alternative architectures. This underscores the importance of acknowledging the limitations in the range of models tested, highlighting potential avenues for future research to explore a more comprehensive spectrum of neural network architectures.

Lastly, yet another aspect that required careful consideration was the possible bias of the human specialists performing the segmentation of the areas of interest. In this regard, we have devised a system meant to

minimize the potential issues: three individuals—comprising a radiology resident (V.O.B.), a radiology fellow (G.M.C.), and a radiology attending physician (C.M.)—leveraged their cumulative 25 years of experience in renal cell carcinoma imaging to manually segment the dataset using 3D Slicer [29].

## 5. Conclusions

This study concludes that data pre-processing is essential for key performance indicator analysis. With meticulous care, time series segmentation, filtering, artefact detection, and region identification were performed during pre-processing. Initial anonymization aimed to safeguard patient privacy and data security. Regardless of the goal, various methods were used to partition regions and mark patients for tumor identification. Developing and using the DICOM- and NIfTI-based YML tool required a large initial investment. Its necessity in improving data analysis and model evaluation has been shown. KPIs provided a detailed assessment of the model's clinical efficacy. The model tried to achieve a Dice score of 0.8 to segment the kidneys precisely, proving its precision. Additionally, the model's precision in categorizing patients with clear renal cell carcinoma (cRCC) was assessed, focusing on accuracy. The KPI "time-to-diagnose" highlighted the efficiency advantages that machine learning can bring to renal clear cell carcinoma diagnosis. In conclusion, these key KPIs demonstrate the model's clinical efficacy in renal cell cancer diagnosis. A thorough review of key performance indicators (KPIs) and suitable data modification procedures before analysis are crucial to determining how effectively a model works and how it can improve radiology and oncology patient care. In light of the above, this study highlights the vital role of careful data preparation in assessing a model's effectiveness in diagnosing kidney cancer. The findings emphasize the importance of using specific measures, such as a Dice score of 0.8 and efficient diagnosis time, to gauge and enhance the model's performance for improved patient care.

**Author Contributions:** Conceptualization, V.-O.B. and C.M.; Data curation, M.S., E.S. and M.G.C.;

Formal analysis, A.-S., C.R., M.G.C. and R.-A.D.; Funding acquisition, G.D.R.; Investigation, M.S., E.S., A.-S., C.R. and G.D.R.; Methodology, V.-O.B., E.S. and M.G.C.; Project administration, C.M., L.S.C.M. and

V.J.; Resources, A.-S. .C.R.; Software, M.S.; Validation, C.M., L.S.C.M. and V.J.; Writing—review and editing, V.-O.B., C.M., R.-A.D., L.S.C.M. and V.J., C.M. has equal contributions to the first author. All authors have read and agreed to the published version of the manuscript.

**Funding:** DeepHealth Project: This project has received funding from the European Union’s Horizon 2020 research and innovation programme under grant agreement No. 825111.

**Institutional Review Board Statement:** The study was peer-validated and approved by the Ethics Committee of the “Profesor Dr. Th. Burghele” Clinical Hospital, Bucharest, Romania (approval number 2/2021), and all procedures in the study respected the ethical standards of the Helsinki Declaration.

**Informed Consent Statement:** Informed consent was obtained from all subjects involved in the study.

**Data Availability Statement:** The data are not publicly available due to the contract of grant agreement No. 825111.

**Acknowledgments:** The technical expertise was provided by SIMAVI. The publication of this paper was supported by the University of Medicine and Pharmacy Carol Davila, through the institutional program Publish not Perish.

**Conflicts of Interest:** The authors declare no conflict of interest. Robert-Andrei Dobran is an employee of the company SIMAVI.

## References

1. Warren, A.Y.; Harrison, D. WHO/ISUP classification, grading and pathological staging of renal cell carcinoma: Standards and controversies. *World J. Urol.* **2018**, *36*, 1913–1926. [[CrossRef](#)] [[PubMed](#)]
2. Capitanio, U.; Bensalah, K.; Bex, A.; Boorjian, S.A.; Bray, F.; Coleman, J.; Gore, J.L.; Sun, M.; Wood, C.; Russo, P. Epidemiology of Renal Cell Carcinoma. *Eur. Urol.* **2019**, *75*, 74–84. [[CrossRef](#)] [[PubMed](#)]
3. Padala, S.A.; Barsouk, A.; Thandra, K.C.; Saginala, K.; Mohammed, A.; Vakiti, A.; Rawla, P.; Barsouk, A. Epidemiology of Renal Cell Carcinoma. *World J. Oncol.* **2020**, *11*, 79–87. [[CrossRef](#)] [[PubMed](#)]

4. Kowalewski, K.-F.; Egen, L.; Fischetti, C.E.; Puliatti, S.; Juan, G.R.; Taratkin, M.; Ines, R.B.; Abate, M.A.S.; Mühlbauer, J.; Wessels, F.; et al. Artificial intelligence for renal cancer: From imaging to histology and beyond. *Asian J. Urol.* **2022**, *9*, 243–252. [[CrossRef](#)] [[PubMed](#)]
5. Chin, A.I.; Lam, J.S.; Figlin, R.A.; Belldegrun, A.S. Surveillance strategies for renal cell carcinoma patients following nephrectomy. *Rev. Urol.* **2006**, *8*, 1–7.
6. Ljungberg, B.; Albiges, L.; Abu-Ghanem, Y.; Bensalah, K.; Dabestani, S.; Fernández-Pello, S.; Giles, R.H.; Hofmann, F.; Hora, M.; Kuczyk, M.A.; et al. European Association of Urology Guidelines on Renal Cell Carcinoma: The 2019 Update. *Eur. Urol.* **2019**, *75*, 799–810. [[CrossRef](#)]
7. Vogel, C.; Ziegelmeüller, B.; Ljungberg, B.; Bensalah, K.; Bex, A.; Canfield, S.; Giles, R.H.; Hora, M.; Kuczyk, M.A.; Merseburger, A.S.; et al. Imaging in Suspected Renal-Cell Carcinoma: Systematic Review. *Clin. Genitourin. Cancer* **2019**, *17*, e345–e355. [[CrossRef](#)] [[PubMed](#)]
8. Du, W.; He, B.; Luo, X.; Chen, M. Diagnostic Value of Artificial Intelligence Based on CT Image in Benign and Malignant Pulmonary Nodules. *J. Oncol.* **2022**, *2022*, 5818423. [[CrossRef](#)]
9. Litjens, G.; Kooi, T.; Bejnordi, B.E.; Setio, A.A.A.; Ciompi, F.; Ghafoorian, M.; Van Der Laak, J.A.W.M.; Van Ginneken, B.; Sánchez, C.I. A survey on deep learning in medical image analysis. *Med. Image Anal.* **2017**, *42*, 60–88. [[CrossRef](#)]
10. Chartrand, G.; Cheng, P.M.; Vorontsov, E.; Drozdal, M.; Turcotte, S.; Pal, C.J.; Kadoury, S.; Tang, A. Deep Learning: A Primer for Radiologists. *RadioGraphics* **2017**, *37*, 2113–2131. [[CrossRef](#)]
11. Soffer, S.; Ben-Cohen, A.; Shimon, O.; Amitai, M.M.; Greenspan, H.; Klang, E. Convolutional Neural Networks for Radiologic Images: A Radiologist’s Guide. *Radiology* **2019**, *290*, 590–606. [[CrossRef](#)] [[PubMed](#)]
12. Yamashita, R.; Nishio, M.; Do, R.K.G.; Togashi, K. Convolutional neural networks: An overview and application in radiology. *Insights Imaging* **2018**, *9*, 611–629. [[CrossRef](#)] [[PubMed](#)]

13. Samek, W.; Wiegand, T.; Müller, K.-R.; Intelligence, E.A. Visualizing and Interpreting Deep Learning Models. *arXiv* **2017**, arXiv:1708.08296. [[CrossRef](#)]
14. Haenssle, H.A.; Fink, C.; Schneiderbauer, R.; Toberer, F.; Buhl, T.; Blum, A.; Kalloo, A.; Hassen, A.B.H.; Thomas, L.; Enk, A.; et al. Man against machine: Diagnostic performance of a deep learning convolutional neural network for dermoscopic melanoma recognition in comparison to 58 dermatologists. *Ann. Oncol.* **2018**, *29*, 1836–1842. [[CrossRef](#)] [[PubMed](#)]
15. Sudre, C.H.; Li, W.; Vercauteren, T.; Ourselin, S.; Cardoso, M.J. Generalised Dice Overlap as a Deep Learning Loss Function for Highly Unbalanced Segmentations. In *Deep Learning in Medical Image Analysis and Multimodal Learning for Clinical Decision Support*; Cardoso, M.J., Arbel, T., Carneiro, G., Syeda-Mahmood, T., Tavares, J.M.R.S., Moradi, M., Bradley, A., Greenspan, H., Papa, J.P., Madabhushi, A., et al., Eds.; Springer International Publishing: Cham, Switzerland, 2017; pp. 240–248. [[CrossRef](#)]
16. The 2021 Kidney Tumor Segmentation Challenge, (n.d.). Available online: <https://kits-challenge.org/kits21/> (accessed on 26 October 2023).
17. Zhao, Z.; Chen, H.; Wang, L. A Coarse-to-Fine Framework for the 2021 Kidney and Kidney Tumor Segmentation Challenge. In *Kidney Kidney Tumor Segmentation*; Heller, N., Isensee, F., Trofimova, D., Tejpaul, R., Papanikolopoulos, N., Weight, C., Eds.; Springer International Publishing: Cham, Switzerland, 2022; pp. 53–58. [[CrossRef](#)]
18. Wen, J.; Li, Z.; Shen, Z.; Zheng, Y.; Zheng, S. Squeeze-and-Excitation Encoder-Decoder Network for Kidney and Kidney Tumor Segmentation in CT Images. In *Kidney Kidney Tumor Segmentation*; Heller, N., Isensee, F., Trofimova, D., Tejpaul, R., Papanikolopoulos, N., Weight, C., Eds.; Springer International Publishing: Cham, Switzerland, 2022; pp. 71–79. [[CrossRef](#)]
19. Gong, Z.; Kan, L. Segmentation and classification of renal tumors based on convolutional neural network. *J. Radiat. Res. Appl. Sci.* **2021**, *14*, 412–422. [[CrossRef](#)]
20. Alzu'bi, D.; Abdullah, M.; Hmeidi, I.; AlAzab, R.; Gharaibeh, M.; El-Heis, M.; Almotairi, K.H.; Forestiero, A.; Hussein, A.M.;

- Abualigah, L. Kidney Tumor Detection and Classification Based on Deep Learning Approaches: A New Dataset in CT Scans. *J. Healthc. Eng.* **2022**, 2022, 3861161. [[CrossRef](#)] [[PubMed](#)]
21. Deep Health—Deep-Learning and HPC to Boost Biomedical Applications for Health, (n.d.). Available online: <https://deephealthproject.eu/> (accessed on 26 October 2023).
  22. Del Rio, M.; Lianas, L.; Aspegren, O.; Busonera, G.; Versaci, F.; Zelic, R. AI Support for Accelerating Histopathological Slide Examinations of Prostate Cancer in Clinical Studies. In *Image Analysis and Processing*; Mazzeo, P.L., Frontoni, E., Sclaroff, S., Distante, C., Eds.; ICIAP 2022 Workshops. ICIAP 2022. Lecture Notes in Computer Science; Springer: Cham, Switzerland, 2022; Volume 13373. [[CrossRef](#)]
  23. Giovanetti, A.; Canalini, L.; Perliti Scorzoni, P. A Compact Deep Ensemble for High Quality Skin Lesion Classification. In *Image Analysis and Processing*; Mazzeo, P.L., Frontoni, E., Sclaroff, S., Distante, C., Eds.; ICIAP 2022 Workshops. ICIAP 2022. Lecture Notes in Computer Science; Springer: Cham, Switzerland, 2022; Volume 13373. [[CrossRef](#)]
  24. Carrión, S.; López-Chilet, Á.; Martínez-Bernia, J.; Coll-Alonso, J.; Chorro-Juan, D.; Gómez, J.A. Automatic Detection of Epileptic Seizures with Recurrent and Convolutional Neural Networks. In *Image Analysis and Processing*; Mazzeo, P.L., Frontoni, E., Sclaroff, S., Distante, C., Eds.; ICIAP 2022 Workshops. ICIAP 2022. Lecture Notes in Computer Science; Springer: Cham, Switzerland, 2022; Volume 13373. [[CrossRef](#)]
  25. Ronneberger, O.; Fischer, P.; Brox, T. U-Net: Convolutional Networks for Biomedical Image Segmentation. *arXiv* **2015**, arXiv.1505.04597. [[CrossRef](#)]
  26. What is Overfitting?—Overfitting in Machine Learning Explained-AWS, (n.d.). Available online: <https://aws.amazon.com/whatis/overfitting/> (accessed on 26 October 2023).
  27. Cancilla, M.; Canalini, L.; Bolelli, F.; Allegretti, S.; Carrion, S.; Paredes, R.; Gomez, J.A.; Leo, S.; Piras, M.E.; Pireddu, L.; et al. The DeepHealth Toolkit: A Unified Framework to Boost Biomedical Applications. In Proceedings of the 2020 25th International Conference

on Pattern Recognition. ICPR, Milan, Italy, 10–15 January 2021; IEEE: New York, NY, USA, 2021; pp. 9881–9888. [\[CrossRef\]](#)

28. Harvey, H.B.; Hassanzadeh, E.; Aran, S.; Rosenthal, D.I.; Thrall, J.H.; Abujudeh, H.H. Key Performance Indicators in Radiology: You Can't Manage What You Can't Measure. *Curr. Probl. Diagn. Radiol.* **2016**, *45*, 115–121. [\[CrossRef\]](#)

29. Fedorov, A.; Beichel, R.; Kalpathy-Cramer, J.; Finet, J.; Fillion-Robin, J.C.; Pujol, S.; Bauer, C.; Jennings, D.; Fennessy, F.; Sonka, M.; et al. 3D Slicer as an image computing platform for the Quantitative Imaging Network. *Magn. Reason. Imaging* **2012**, *30*, 1323–1341. [\[CrossRef\]](#)

**Disclaimer/Publisher's Note:** The statements, opinions and data contained in all publications are solely those of the individual author(s) and contributor(s) and not of MDPI and/or the editor(s). MDPI and/or the editor(s) disclaim responsibility for any injury to people or property resulting from any ideas, methods, instructions or products referred to in the content.

## Appendix 2



Journal of  
*Imaging*



Correction

---

Correction: Bolocan et al.  
Convolutional Neural Network  
Model for Segmentation and  
Classification of Clear Cell Renal  
Cell Carcinoma Based on  
Multiphase CT Images. *J. Imaging*  
2023, 9, 280

---

Vlad-Octavian Bolocan, Mihaela Secareanu, Elena Sava, Cosmin  
Medar,  
Loredana Sabina Cornelia Manolescu, Alexandru-Ștefan Cătălin Rașcu,  
Maria Glencora Costache,  
George Daniel Radavoi, Robert-Andrei Dobran and Viorel Jinga

Correction

**Correction: Bolocan et al. Convolutional Neural Network Model for Segmentation and Classification of Clear Cell Renal Cell**

**Carcinoma Based on Multiphase CT Images. *J. Imaging* 2023, 9, 280**

**Vlad-Octavian Bolocan<sup>1,2</sup>, Mihaela Secareanu<sup>2</sup>, Elena Sava<sup>2</sup>, Cosmin Medar<sup>1,2</sup>,  
Loredana Sabina Cornelia Manolescu<sup>1,\*</sup>, Alexandru-S, tefan Cătălin Ras,  
cu<sup>3,4</sup>, Maria Glencora Costache<sup>1</sup>, George Daniel Radavoi<sup>3,4</sup>, Robert-Andrei  
Dobran<sup>5</sup> and Viorel Jinga<sup>3,4,6</sup>**



[10.3390/jimaging10020035](https://doi.org/10.3390/jimaging10020035)

**Citation:** Bolocan, V.-O.; Secareanu, M.; Sava, E.; Medar, C.;

Received: 17 January 2024

Accepted: 19 January 2024

Published: 29 January 2024



Manolescu, L.S.C.; Ras,cu, A.-S, .C.; Costache, M.G.; Radavoi, G.D.; Dobran, R.-A.; Jinga, V.

**Copyright:** © 2024 by the authors. Licensee MDPI, Basel, Switzerland. This article is an open access article distributed under the terms and conditions of the Creative Commons Attribution (CC BY) license (<https://creativecommons.org/licenses/by/4.0/>).

Correction:  
Bolocan et al.  
Convolutional  
Neural Network  
Model for  
Segmentation and  
Classification of  
Clear Cell Renal  
Cell  
Carcinoma Based  
on Multiphase CT  
Images. *J. Imaging*  
2023, 9, 280. *J.*  
*Imaging* 2024, 10,  
35. <https://doi.org/>

<sup>1</sup> Department of Fundamental Sciences, Faculty of Midwifery and Nursing, University of Medicine and Pharmacy “Carol Davila”, 050474 Bucharest, Romania; vlad-octavian.bolocan@drd.umfcd.ro (V.-O.B.); cosmin.medar@umfcd.ro (C.M.); maria.costache@umfcd.ro (M.G.C.)

<sup>2</sup> Department of Clinical Laboratory of Radiology and Medical Imaging, Clinical Hospital “Prof. Dr. Theodor Burghele”, 050664 Bucharest, Romania; mihaela.secareanu@rez.umfcd.ro (M.S.); elena.sava@rez.umfcd.ro (E.S.)

<sup>3</sup> Department of Urology, Clinical Hospital “Prof. Dr. Theodor Burghele”, Faculty of Medicine, University of Medicine and Pharmacy “Carol Davila”, 050474 Bucharest, Romania; stefan.rascu@umfcd.ro (A.-S, .C.R.); daniel.radavoi@umfcd.ro (G.D.R.); viorel.jinga@umfcd.ro (V.J.)

<sup>4</sup> Department of Urology, Clinical Hospital “Prof. Dr. Theodor Burghele”, 050664 Bucharest, Romania

<sup>5</sup> Software Imagination & Vision (Simavi), 013685 Bucharest, Romania; robert.dobran@simavi.ro

<sup>6</sup> Medical Sciences Section, Academy of Romanian Scientists, 050085 Bucharest, Romania

\* Correspondence: loredana.manolescu@umfcd.ro

been deleted in the References section.

In the last paragraph of the Discussion, the citation should be updated as follows:

“Lastly, yet another aspect that required careful consideration was the possible bias of the human specialists performing the segmentation of the areas of interest. In this regard, we have devised a system meant to minimize the potential issues: three individuals—comprising a radiology resident (V.O.B.), a radiology fellow (G.M.C.), and a radiology attending physician (C.M.)—leveraged their cumulative 25 years of experience in renal cell carcinoma imaging to manually segment the dataset using 3D Slicer [29]”.

The authors state that the scientific conclusions are unaffected. This correction was approved by the Academic Editor. The original publication has also been updated.

#### Reference

1. Bolocan, V.-O.; Secareanu, M.; Sava, E.; Medar, C.; Manolescu, L.S.C.; Cătălin Ras, cu, A.-S. ; Costache, M.G.; Radavoi, G.D.; Dobran, R.-A.; Jinga, V. Convolutional Neural Network Model for Segmentation and Classification of Clear Cell Renal Cell Carcinoma Based on Multiphase CT Images. *J. Imaging* **2023**, *9*, 280. [[CrossRef](#)] [[PubMed](#)]

**Disclaimer/Publisher’s Note:** The statements, opinions and data contained in all publications are solely those of the individual author(s) and contributor(s) and not of MDPI and/or the editor(s). MDPI and/or the editor(s) disclaim responsibility for any injury to people or property resulting from any ideas, methods, instructions or products referred to in the content.

---

In the original publication [1], references “[30–37]” were cited by mistake. The citations have now

---

*J. Imaging* **2024**, *10*, 35.  
<https://doi.org/10.3390/jimaging10020035>  
<https://www.mdpi.com/journal/jimaging>

## Appendix 3

### Open Access Review Article

DOI: 10.7759/cureus.57087

**Review began** **A Pictorial Review**

03/19/2024 [1](#), [2](#) [1](#) [1](#)

**Review ended** [Vlad-Octavian Bolocan](#) , [Georgian-Florentin Diaconu](#) ,  
03/19/2024 [Mihaela Secareanu](#) ,

**Published** [2](#) [3](#), [4](#), [5](#) [2](#) [6](#)

03/27/2024 [Loredana Sabina Cornelia Manolescu](#) , [Viorel Jinga](#) ,

© **Copyright** [Maria-Glencora Costache](#) , [Gelu Adrian Popa](#) ,

2024 [1](#), [2](#)

Bolocan et al. [Cosmin Medar](#)

This is an open access article distributed under the terms of the Creative Commons Attribution License CC-BY 4.0., which permits unrestricted use, distribution, and reproduction in any medium, provided the original author and source are credited.

1. Department of Clinical Laboratory of Radiology and Medical Imaging, Clinical Hospital “Prof. Dr. Theodor Burghele”, Bucharest, ROU 2. Department of Fundamental Sciences, Faculty of Midwifery and Nursing, University of Medicine and Pharmacy “Carol Davila”, Bucharest, ROU 3. Department of Urology, Clinical Hospital “Prof. Dr. Theodor Burghele”, Bucharest, ROU 4. Department of Urology, Faculty of Medicine, University of Medicine and Pharmacy “Carol Davila”, Bucharest, ROU 5. Medical Sciences Section, Academy of Romanian Scientists, Bucharest, ROU 6. Department of Radiology and Medical Imaging, Clinical Hospital of Emergency “Sf Ioan”, Bucharest, ROU

**Corresponding author:** Loredana Sabina Cornelia Manolescu, loredana.manolescu@umfcd.ro

---

---

**Renal Sinus Abstract**

**Pathologies** Diverse conditions comprise the spectrum of renal sinus pathologies, which have diagnostic and therapeutic implications for patients. Using CT imaging as a lens, this exhaustive review examines the representation of these

**Depicted by CT Imaging:**

pathologies. The article begins with a concise synopsis of renal anatomy and the specialized CT methodologies utilized to achieve excellent visualization.

Transformational cell carcinoma, leiomyosarcoma, renal cell carcinoma, multilocular nephroma, and lymphoma are among the tumoral origins of the renal sinus pathologies that are investigated. Further, vascular pathologies including fistulas, hematomas, and aneurysms are included in the discourse, along with parapelvic and peripelvic cysts, and lipomatosis. In addition to urolithiasis and

encrusted uretero-pyelitis, the review examines the consequences of metal toxicity and non-neoplastic conditions. With a focus on critical CT imaging findings that aid in the provision of an accurate diagnosis, every pathology is meticulously examined. With the intention of improving clinical decision-making and patient care, this article intends to function as a valuable resource for radiologists, clinicians, and researchers who are engaged in the interpretation and comprehension of renal sinus pathologies.

---

**Categories:** Pathology, Radiology, Urology

**Keywords:** metal toxicity, urolithiasis, tumours, imaging, renal sinus pathologies

## **Introduction And Background**

### **Anatomy**

The renal sinus is a spacious central cavity that arises from the expansion of the perinephric space into a profound recess located at the core of the kidney. It is enveloped by the renal tissue on the lateral aspects. The renal sinus houses the primary branches of the renal artery and vein, as well as the major and minor calyces of the collecting system. It also contains fat, lymphatic veins, nerve fibers of the autonomic nervous system, as well as various quantities of fibrous tissue. Consequently, the different elements of the renal sinus might give birth to distinct clinical diseases. Moreover, the renal sinus can also be indirectly affected by clinical diseases that include the surrounding renal tissue and neighboring retroperitoneal regions [1-3].

### **Technique**

The utilization of CT has evolved into an essential procedure for diagnosing renal sinus pathologies. A CT scan offers a thorough assessment of the renal sinus as well as its adjacent anatomical components, such as the collecting system, medulla, and cortex. The examination may be conducted with or without IV contrast; the

selection of the contrast agent and the scheduling of the scan are determined by the particular pathology under investigation. CT scans are highly advantageous in two situations: identifying calcifications (e.g., urolithiasis) and evaluating the renal sinus in instances of heavy metal poisoning (e.g., extensive streaking artifacts caused by metal objects in the body). In addition to the detection of calcifications, CT is also useful for the evaluation of renal sinus hematomas and urinomas. Hematomas appear as amorphous high-density

substances on CT, highly suggestive of fresh blood. Urinomas, on the other hand, are readily demonstrated in contrast-enhanced studies on the excretory phase, due to direct contrast extravasation from the urinary tract. In cases of pyelonephritis, CT can demonstrate the presence of conglomerate inflammatory cells, leading to a pseudotumor within the renal sinus. The presence of encrusted uretero-pyelitis can also be suggested by the specific aspect of calcifications on CT scans. With the combination of these imaging features, CT provides a comprehensive evaluation of renal sinus pathologies, enabling prompt and accurate diagnosis and treatment.

## **How to cite this article**

Bolocan V, Diaconu G, Secareanu M, et al. (March 27, 2024) Renal Sinus Pathologies Depicted by CT Imaging: A Pictorial Review. *Cureus* 16(3): e57087. DOI 10.7759/cureus.57087

CT is becoming a useful tool for diagnosing and treating renal sinus tumors. CT enables the evaluation of the dimensions, position, and correlation of the abnormality with nearby structures, as well as the identification of any potential spread into neighboring tissues or organs. Giving contrast material through an IV makes the lesion and the tissues around it clearer, making it easier to tell the difference between it and other structures and giving important information for getting ready for surgery.

Furthermore, CT can assist in distinguishing between harmless and cancerous growths, as well as offer insights into the severity of the cancer and its impact on the renal sinus vasculature. It is crucial to consider this specifically for the staging and therapy of renal cell carcinomas, which are the predominant form of renal malignancy and frequently arise in the renal sinus. A CT exam allows for the evaluation of tumor vascularity, necrosis, and hemorrhage, as well as provides crucial prognostic data.

Lesions involving the renal sinus can be classified as either non-neoplastic or neoplastic, similar to other anatomical areas. Tumors that affect the renal sinus can be classified into several categories based on their site of origin. These include tumors originating from the renal pelvis, tumors that spread from the renal parenchyma into the renal sinus, primary tumors of mesenchymal origin, and retroperitoneal tumors that ultimately impact the renal sinus. Non-tumorous conditions like lipomatosis, vascular lesions, cysts, and fluid collections, which can be either inflammatory or non-inflammatory, can affect the renal sinus [4].

## **Review**

### **Tumors**

Various benign and malignant neoplasms can affect the renal sinus, either directly from it or via the surrounding cortex or retroperitoneum. The presence of fat in the renal sinus is useful in detecting tiny cancers. Observing the fat in the renal sinus can help identify the presence of a tumor and determine its stage. The presence or absence of fat can help diagnose and manage renal sinus neoplasms [1,3,5]. Only around 5% of

urinary tract neoplasms are caused by malignant tumors in the renal pelvis.

### **Transitional cell carcinomas (TCCs)**

TCCs account for 95% of all uroepithelial tumors in the renal pelvis. The remaining 5% consists of squamous cell carcinoma (the majority) and adenocarcinoma. TCCs can have one of two shapes: papillary (more than 85% of tumors) or non-papillary (tumors that are sessile or nodular, high-grade, and invade beyond the mucosa early). Papillary tumors have frond-like projections and are low-grade, with invasion beyond the mucosa happening later. Patients often appear with microscopic or macroscopic hematuria. If the tumor is in the pelviureteric junction, hydronephrosis symptoms, like pain in the flank, may be the first sign. Clots related to the condition may cause symptoms like those of renal calculi. Some people seek medical assistance only after their metastatic disease produces symptoms, such as constitutional symptoms or symptoms caused by a specific metastatic deposit [6].

TCCs (Figure 1) typically have soft tissue density (8-30 Hounsfield units (HU)) and modest enhancement, which is less pronounced than renal parenchyma or renal cell carcinoma. These tumors are typically located in the renal pelvis rather than the renal parenchyma and can range in size from minor filling deficiencies to massive masses that obliterate the renal sinus fat. Large infiltrating transitional cell carcinomas, as opposed to renal cell carcinomas, have normal renal morphology. Larger tumors may contain zones of necrosis. A small soft tissue mass should be sought in situations of minor tumors near the pelviureteric junction, which result in hydronephrosis. The calyces are usually dilated, and the renal pelvis wall can be thickened. Small calcifications may occasionally appear on the surface of papillary projections [7,8].



**FIGURE 1: The contrast-enhanced CT (CECT) images during the arterial (a), nephrographic (b), and urographic (c) phases demonstrate the faceless kidney, which appears enlarged and displays a high density of soft tissue. Furthermore, the enhancement of the**

renal vein is modest due to tumoral invasion accompanied by indications of thrombosis. Large infiltrating transitional cell carcinomas (TCCs), as opposed to renal cell carcinomas (RCC), do not alter the kidney's inherent contour. Additionally, obliteration and amputation of the pyelocaliceal system are noted, which serve as indications of substantial pathological alterations occurring within the renal structure.

This figure is a republished image, permission was obtained from the original publisher, <https://epos.myesr.org/poster/esr/ecr2018/C-2802>

---

During the initial phases of transitional cell carcinoma of the kidney (stage I or II), a solid mass forms in the center of the renal pelvis. This mass grows outward, putting pressure on the fat in the renal sinus and creating a visible separation from the renal parenchyma. This separation can be observed either through the presence of renal sinus fat or contrast material used in imaging. The disease gets worse in stages III and IV, though, and transitional cell carcinoma (TCC) spreads to the nearby renal parenchyma. This causes the renal sinus fat to disappear completely (Figure 2). Despite this, the natural form of the kidney is usually maintained [8].



**FIGURE 2:** The contrast-enhanced CT (CECT) scan conducted during the arterial phase in the axial plane reveals a kidney devoid of distinguishable facial features, a characteristic manifestation attributed to transitional cell carcinoma (TCC) with infiltration into the sinus fat. Furthermore, notable within the imaging and indicated by the small arrow is the identification of renal artery stenosis, a condition induced by calcifications.

This figure is the original work of the authors. Patient consent for the use of the image was obtained, as mentioned in the patient consent form (point no. 12).

---

### **Squamous cell carcinoma**

Squamous cell carcinoma constitutes 1-7% of neoplasms in the upper urinary system. It is frequently associated with persistently infected staghorn calculi. Individuals afflicted with this syndrome typically exhibit advanced tumors that are poorly to moderately differentiated. The imaging characteristics of squamous cell carcinomas closely resemble those of transitional cell carcinomas. The presence of kidney stones in the past and chronic inflammation of the urothelium are significant factors that contribute to the development of squamous cell carcinoma. There may be squamous cell carcinoma present if there is a renal stone, a large renal sinus component, and an infiltrating lesion that looks like it is spread out geographically [9].

### **Adenocarcinoma**

Adenocarcinoma comprises less than 1% of upper urinary tract malignancies. An adenocarcinoma may have a connection to calculi and long-term obstruction, since these symptoms may exist in patients with this type [10].

### **Mesenchymal tumors**

Mesenchymal tumors are neoplasms that arise from pluripotent cells with the ability to differentiate into various types of mesenchymal tissues, including blood vessels, fibrous tissue, adipose tissue, and others. Adult renal mesenchymal tumors can originate in the renal sinus space, renal capsule, or renal parenchyma and can exhibit either benign or malignant characteristics. Angiomyolipoma, leiomyoma, and lipoma are instances of noncancerous mesenchymal tumors. Leiomyosarcoma (Figure 3) angiosarcoma, and malignant fibrous histiocytoma are types of malignant mesenchymal tumors [11].

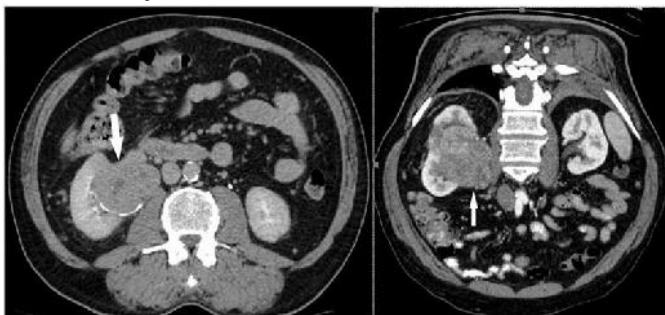


**FIGURE 3: The axial contrast-enhanced CT (CECT) scan performed during the excretory phase and the coronal oblique scan conducted during the arterial phase both unveil the presence of a histologically confirmed leiomyosarcoma of the inferior vena cava (IVC). This pathology manifests as a substantial heterogeneous mass, predominantly owing to central necrosis, which exhibits diminished enhancement compared to the tumoral tissue. Additionally, the imaging reveals the invasion of the right renal sinus and right renal parenchyma by the sarcoma, resulting in a discernible mass effect on the collecting system. These observations collectively depict the intricate nature of the leiomyosarcoma, highlighting its propensity for invasion and its consequential impact on adjacent anatomical structures within the renal vicinity.**

This figure is the original work of the authors. Patient consent for the use of the image was obtained, as mentioned in the patient consent form (point no. 12).

---

Imaging studies can produce ambiguous outcomes when diagnosing these rare malignancies. Nevertheless, MRI possesses a clear superiority over CT scans in precisely depicting the extent of infiltration into the renal vein and inferior vena cava. CT scans may typically identify the presence of a mesenchymal tumor in the renal sinus. These images usually show a clear boundary between the tumor and the renal collecting system, as well as compression of the renal pelvis and calyces. Enhanced CT scans can also visualize constricted blood arteries in the renal hilum. Additionally, during the excretory phase of the scan, a compressed renal pelvis and calyces may be observed without any abnormalities in the filling process.

### **Parenchymal tumors**

Most tumors that originate from the renal parenchyma grow by expanding and appearing as round masses. These tumors can also press against or infiltrate the renal sinus fat as they grow toward the renal pelvis. The common examples of these tumors are renal cell carcinoma (RCC) and benign multilocular cystic nephroma (MCN).

#### *RCC*

RCC is the most prevalent type of malignant renal tumor (Figure 4 and Figure 5); RCC is a primary malignant adenocarcinoma that originates from the renal tubular epithelium. On imaging tests, RCC can appear in

different forms, from being solid and uniform to having areas of necrosis, cystic change, and hemorrhage.



**FIGURE 4: During the arterial (a) and urographic (b) phases of contrastenhanced CT (CECT), a comprehensive evaluation unveils a considerable, expansive, and heterogenous soft-tissue lesion centrally situated within the left kidney. Notably, this lesion demonstrates invasion into the renal sinus. The heterogeneous appearance of the mass is attributable to variable enhancement patterns, with heightened enhancement evident in the periphery juxtaposed against lower enhancement centrally, which corresponds to areas of necrosis within the tumor. These characteristic features align closely with the diagnostic criteria for renal cell carcinoma (RCC). The left renal vein is marked by the asterisk at the renal sinus level.**

This figure is the original work of the authors. Patient consent for the use of the image was obtained, as mentioned in the patient consent form (point no. 12).

---

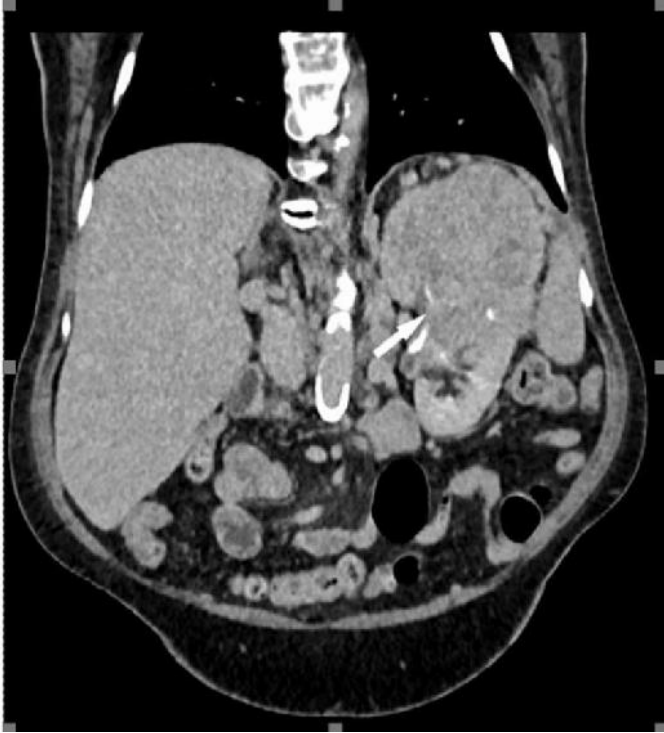


**FIGURE 5: Coronal oblique urographic contrast-enhanced CT (CECT) phase presents a striking visual representation of a substantial mass originating from the upper two-thirds of the left kidney. This voluminous lesion exhibits characteristics indicative of necrosis, further emphasizing its significant size and advanced pathology. Notably, the mass is depicted invading the renal sinus.**

This figure is the original work of the authors. Patient consent for the use of the image was obtained, as mentioned in the patient consent form (point no. 12).

---

Most cases of RCC grow by expansion and can often extend into the renal pelvis, causing focal hydronephrosis or displacement of the caliceal. In contrast to TCC, RCC has a tendency to spread into the venous system [12].

Three-dimensional CT or MR imaging can provide detailed information about the location of the renal mass, its relationship with the collecting system, and the renal vessels.

#### *MCN*

MCN (Figure 6) is generally characterized by a single cystic mass with multiple compartments, enclosed by a thick fibrous layer and compressing surrounding tissue. Such cysts do not often exhibit calcification, hemorrhage, or necrosis. On CT scans, MCN appears as a large,

multiloculated cystic mass, often extending into the renal pelvis, with septal enhancement that may be inconsistent and without solid enhancements. Perirenal fat may or may not display streakiness [13]. Surgical treatment for MCN typically involves the removal of the affected kidney or a portion of it, along with any impacted lymph nodes.

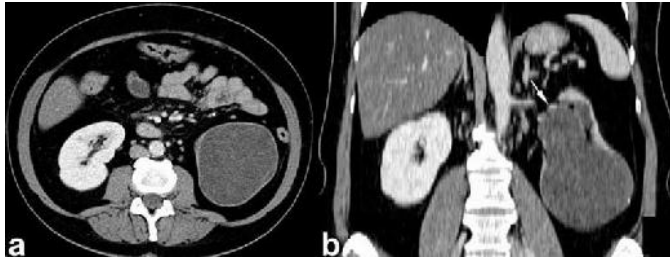


**FIGURE 6: Axial picture (a) and the reconstruction in the frontal plane (b) of a contrast-enhanced CT (CECT) scan during the nephrographic phase unveil a notable pathological finding within the left kidney. Specifically, a multiloculated cystic mass is prominently displayed, indicating the presence of multiple septa. This mass is encapsulated by a robust fibrous capsule, suggestive of a well-defined boundary separating it from the surrounding renal parenchyma. Notably, the presence of this thick fibrous capsule exerts pressure on the adjacent renal parenchyma with cortical thinning. Furthermore, the capsule extends into the renal sinus, as indicated by the arrow, underscoring the invasive nature of the lesion.**

This figure is a republished image, permission was obtained from the original publisher, <https://epos.myesr.org/poster/esr/ecr2018/C-2802>

---

### **Retroperitoneal tumors that extend to the renal sinus**

The renal sinus is part of the perinephric space, so any retroperitoneal tumor can spread to the renal sinus. Several retroperitoneal tumors, including lymphoma, sarcomas, multiple myelomas, and Castleman disease, can directly invade the perinephric space and renal sinus.

On CT scans, retroperitoneal lymphoma appears as an expansive tissue mass that encompasses the perinephric area and renal sinus. The renal vessels remain open despite being surrounded by the tumor, a feature that is typical of lymphoma, and obstructive hydronephrosis is often seen due to the direct involvement of the renal collecting system [14]. This appearance is most common in patients with advanced non-Hodgkin lymphoma (Figure 7).

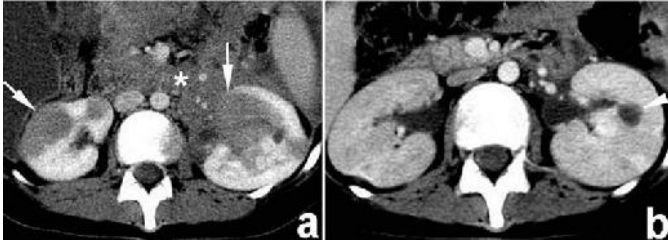


**FIGURE 7:** During the nephrographic phase, contrast-enhanced CT (CECT) imaging was conducted both before (a) and after (b) six months of treatment. The scans reveal the presence of a significant infiltrative mass of soft tissue, denoted by the asterisk, indicative of lymphoblastic lymphoma. According to its infiltrative pattern, the mass extends into the retroperitoneum and invades the renal sinus and parenchyma, as highlighted by the arrows. Following six months of treatment, a subsequent CT scan demonstrates complete resolution of both the renal and retroperitoneal tumors. Notably, attention is drawn to the identification of a small cyst located on the left kidney, denoted by the arrowhead.

This figure is a republished image, permission was obtained from the original publisher, <https://epos.myesr.org/poster/esr/ecr2018/C-2802>

---

Both on CT and ultrasonography, lymphomatous masses are uniform in appearance. CT scans show less enhancement of the mass, and on ultrasonography, lymphoma appears as a hypoechoic mass, reflecting its homogeneous tissue structure.

### **Metastasis**

Metastasis to the sinus lymph nodes can occur either as a widespread retroperitoneal spread or as isolated involvement, as seen with primary gonadal tumors. This is due to the abundance of perforating vessels and lymphatic channels that connect to the renal sinus [15].

### **Lipomatosis**

The renal sinus usually has adipose tissue that surrounds multiple tissues inside it. Renal sinus lipomatosis (Figure 8) is defined as the pathological accumulation of adipose tissue in the renal sinus. The rise in fat content is a prevalent consequence of the aging process as well as a consequence of obesity. However, the rise in fat content can also be attributed to variables such as renal parenchymal shrinkage, inflammation, calculous illness, aging, or exposure to exogenous or endogenous hormones.

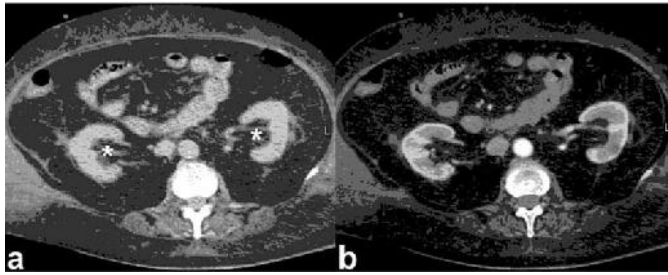


**FIGURE 8:** Non-enhanced CT (NECT) phase (a) and the contrastenhanced CT (CECT) arterial phase (b) showcase the presence of extra pure fat replacement surrounding both sides of the renal sinus, depicted by the asterisk. However, despite the presence of this fat replacement, there is no discernible mass effect and no displacement observed on the urinary collecting system.

This figure is a republished image, permission was obtained from the original publisher, <https://epos.myesr.org/poster/esr/ecr2018/C-2802>

---

Certain individuals exhibit a more pronounced manifestation of massive renal sinus lipomatosis, characterized by the presence of infection, renal calculi, persistent hydronephrosis, and substantial shrinkage of the kidney's parenchyma [16].

Renal replacement lipomatosis is a rare disease in which fat cells grow in the renal sinus and perinephric area. This makes the renal parenchyma shrink and get badly damaged from the constant inflammation. Renal parenchymal atrophy or destruction, perinephric and hilar lipomatosis, renal calculi, and perinephric abscesses that may spread to the psoas muscle are among the characteristics of this illness that are typically shown on CT scans [17].

### **Renal cysts**

Renal sinus cysts are a type of simple cyst that are located within the renal sinus and occur in just 1.28% to 1.5% of autopsy cases [18]. They can be classified into parapelvic (Figure 9 and Figure 10) and peripelvic cysts (Figure 11). Parapelvic cysts come from the adjacent renal tissue and project into the renal sinus, while peripelvic cysts originate within the sinus and have a lymphatic origin [18]. Sometimes, peripelvic cysts can put pressure on the pelvic floor and cause hydronephrosis. On the other hand, peripelvic cysts are usually bilateral and do not affect how the body works. They may be mistaken for hydronephrosis on non-contrast CT scans or ultrasonography but can be differentiated on contrast-enhanced CT scans [19].

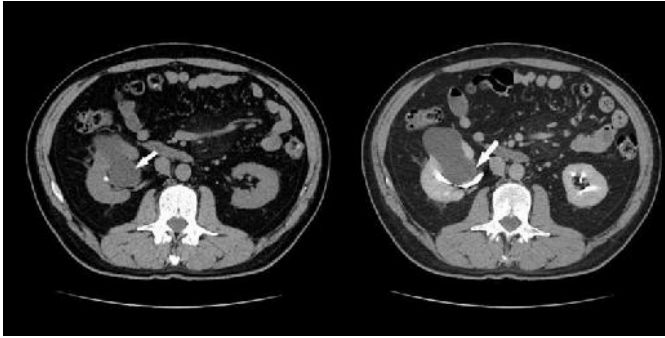


**FIGURE 9: Non-enhanced CT scan (NECT) (a) and contrast-enhanced CT (CECT) scan during the urographic phase (b), a notable observation is evident. Specifically, there is the identification of a right parapelvic cyst, marked by the arrow, which protrudes into the renal sinus from the adjacent tissue. Despite its presence, there is no observed compression or pressure exerted upon the pelvicalyceal system.**

This figure is the original work of the authors. Patient consent for the use of the image was obtained, as mentioned in the patient consent form (point no. 12).

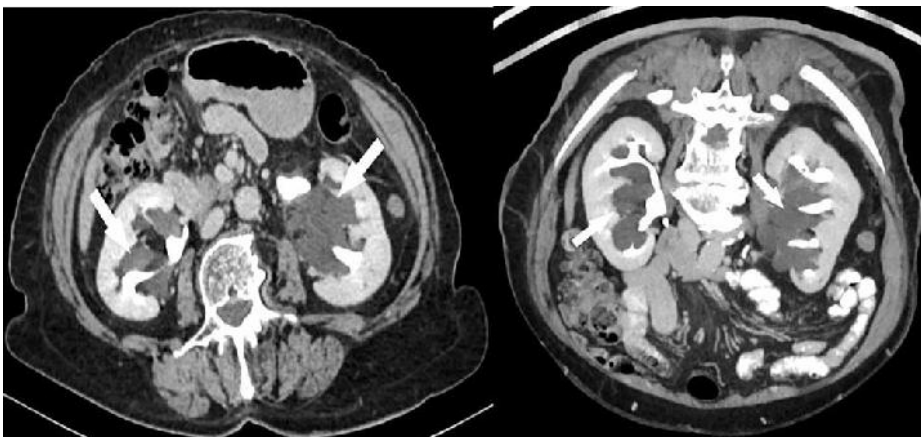


**FIGURE 10: The axial and oblique coronal contrast-enhanced CT (CECT) images captured during the excretory phase reveal multiple cysts, bilaterally distributed and originating within the kidney parenchyma, which are prominently displayed. These parapelvic cysts extend into the renal sinus region, indicating their involvement with the anatomical structures surrounding the kidneys.**

This figure is the original work of the authors. Patient consent for the use of the image was obtained, as mentioned in the patient consent form (point no. 12).

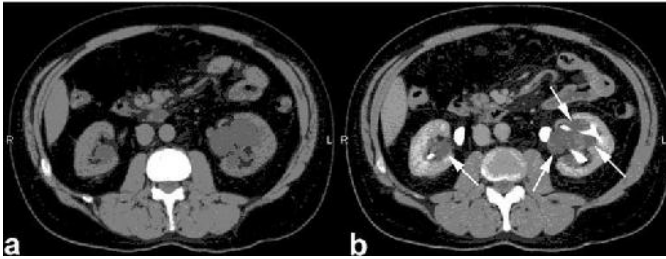


**FIGURE 11: Non-enhanced CT (NECT) (a) and contrast-enhanced CT (CECT) during the urographic phase (b), showcase two peripelvic cysts, indicated by the arrows, which are evident on either side of the renal pelvis. These simple fluid-filled cysts are situated in close proximity to the renal pelvis and infundibula, with no observed compression or constriction of the pelvicalyceal system.**

This figure is the original work of the authors. Patient consent for the use of the image was obtained, as mentioned in the patient consent form (point no. 12).

---

### **Vascular pathologies**

Vascular problems, like renal artery aneurysms (Figure 12), vein-artery connections, renal vein varix, and arteriocaliceal fistula (Figure 13), can affect the renal sinus and show up as pseudocystic lesions near the pelvis. The utilization of contrast-enhanced CT or MRI, color Doppler ultrasound, and angiography can readily detect these conditions.

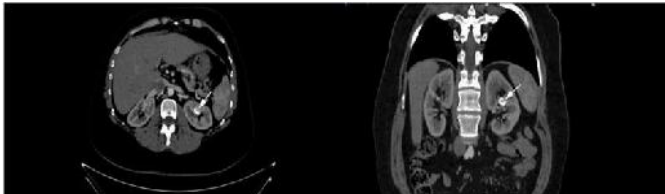


**FIGURE 12: Contrast-enhanced CT (CECT) in the artery phase reveals significant findings in both axial (a) and oblique coronal-plane reconstructions (b). Notably, there is a renal artery saccular aneurysm, indicated by the arrows, which presents as a focal dilation and is engorged with contrast material, characteristic of a saccular aneurysm but with multiple parietal calcifications. This imaging modality provides a detailed visualization of the arterial vasculature, facilitating the precise identification and characterization of pathological conditions such as aneurysms.**

This figure is the original work of the authors. Patient consent for the use of the image was obtained, as mentioned in the patient consent form (point no. 12).



**FIGURE 13:** Non-enhanced CT (NECT) (a) is followed by a contrast-enhanced CT (CECT) scan of the artery (b), and subsequently, the urographic phase (c). In these sequences, an arrow highlights a contrast-filled outpouching detected within a branch of the right renal artery. Notably, blood is observed to be draining into the renal pelvis (asterisk), indicating the presence of a pseudoaneurysm with a fistula in the pyelocaliceal system. Additionally, attention should be paid to the iodinated contrast media that have been flushed out in the anterior portion of the renal pelvis (arrowhead), accentuating the anatomical details and aiding in the characterization of the vascular anomaly.

This figure is a republished image, permission was obtained from the original publisher, <https://epos.myesr.org/poster/esr/ecr2018/C-2802>

There are three types of arteriovenous fistulas in the kidneys: congenital arteriovenous fistulas, which are there at birth; postpartum acquired arteriovenous fistulas (Figure 14), which form after a procedure like a biopsy or an injury; and idiopathic arteriovenous fistulas, whose cause is unknown [20]. The majority of these connections are acquired, with biopsies being the most frequent cause. While aortic-venous connections in the kidneys generally remain asymptomatic, certain individuals may manifest symptoms including but not limited to heavy hemorrhage, abdominal whooshing, heart failure, hypertension, or abdominal discomfort. Depending on the dimensions of these connections, imaging tests may fail to detect them at times [21].

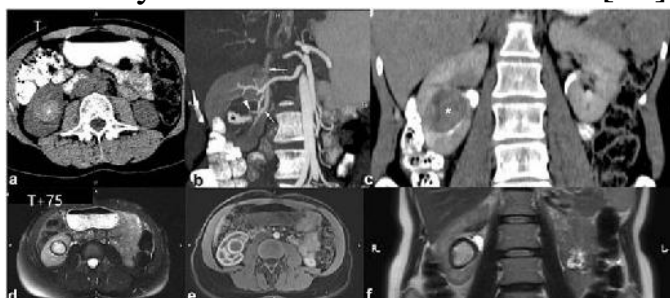


**FIGURE 14:** A comprehensive imaging assessment was conducted using multiple modalities, including non-enhanced CT (NECT) (a),

contrast-enhanced CT (CECT) in the arterial phase with reconstruction in an oblique plane (b), CECT in the urographic phase with reconstruction in the frontal plane (c), MRI axial T2 half-Fourier acquisition single-shot turbo spin echo imaging fat suppression (HASTE FS) (d), MRI axial Volumetric interpolated breath-hold examination (VIBE) post-gadolinium in the arterial phase (e), and MRI coronal T2 half-Fourier acquisition single-shot turbo spin echo imaging (HASTE) (f). In the case of a 35-year-old woman who recently gave birth, abnormalities in renal arteriovenous communication with associated pseudoaneurysms were identified, denoted by black asterisks. Specifically, the feeding artery (arrowhead) and venous drainage (arrows) exhibited notable anomalies, indicative of the presence of pseudoaneurysms. Additionally, a lesion resembling a hematoma in the kidney region was observed, characterized by the presence of spontaneous hyperdensities compatible with acute hemorrhage. Following a 75-day interval, subsequent MRI imaging revealed a significant resolution of the malformation, indicating spontaneous regression. Moreover, the hematoma appeared to have diminished in size.

This figure is a republished image, permission was obtained from the original publisher, <https://epos.myesr.org/poster/esr/ecr2018/C-2802>

---

## Hematomas

Hemorrhage can result from trauma, arteriovenous malformation, or anticoagulant medication. The formation of a renal sinus hematoma, which is characterized by bleeding within the renal sinus, is an unusual side effect of anticoagulant therapy (Figure 15). This problem may emerge in those who have a long prothrombin time. CT scans show the presence of an irregular, thick substance that clearly supports the presence of recent blood and does not amplify when contrast is used [22].

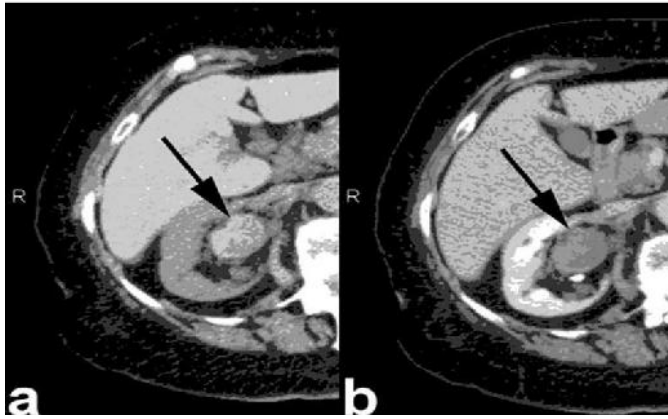


**FIGURE 15: Imaging studies comprising non-enhanced CT (NECT) (a) and contrast-enhanced CT (CECT) during the urographic phase (b). These modalities were utilized to evaluate a rare complication associated with blood thinners: a right kidney sinus hematoma. The NECT scan (a) provided an initial assessment, revealing the presence of a hematoma within the right kidney sinus. Subsequent CECT during the urographic phase (b) further delineated the extent and characteristics of the hematoma, aiding in its precise characterization and assessment of potential complications.**

This figure is a republished image, permission was obtained from the original publisher, <https://epos.myesr.org/poster/esr/ecr2018/C-2802>

---

### **Urinomas**

Urinomas are collections of urine commonly located in the perirenal space in the retroperitoneum. They are usually caused by blockage of the urinary tract, trauma, or after medical instruments are used. In contrast-enhanced studies during the excretory phase, urine leakage can usually be directly seen due to the contrast material extravasating from the urinary tract [23].

### **Urolithiasis**

A common cause of calcifications in the kidney is kidney stones (Figure 16 and Figure 17). One in 10 people is affected at least once during their lifetime [24]. Calcium oxalate is the main component of kidney stones, however demographic and metabolic variables might affect it. A non-contrast CT scan can identify most kidney stones because they are radio-dense despite fluctuations in their density. Uric acid stones have a density of 100-200 HU, while calcium oxalate stones have 400-600 HU.

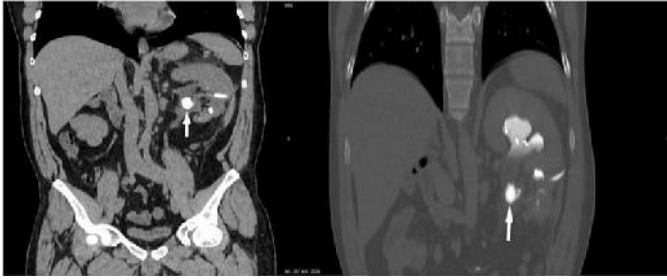


**FIGURE 16: Non-enhanced CT (NECT) (a) and contrast-enhanced CT (CECT) during the urographic phase (b). The NECT scan (a) indicates the presence of a calculus within the left renal pelvis (which also happens to show a duplex collecting system, both pathways being obstructed by the calculus), clearly demarcated by the arrow. Subsequent imaging with CECT during the urographic phase (b) showcases the dilatation of the pelvicalyceal system (hydronephrosis). There are also visible partial fragments of nephrostomy tubes which should not be mistaken for calculi.**

This figure is the original work of the authors. Patient consent for the use of the image was obtained, as mentioned in the patient consent form (point no. 12).

---

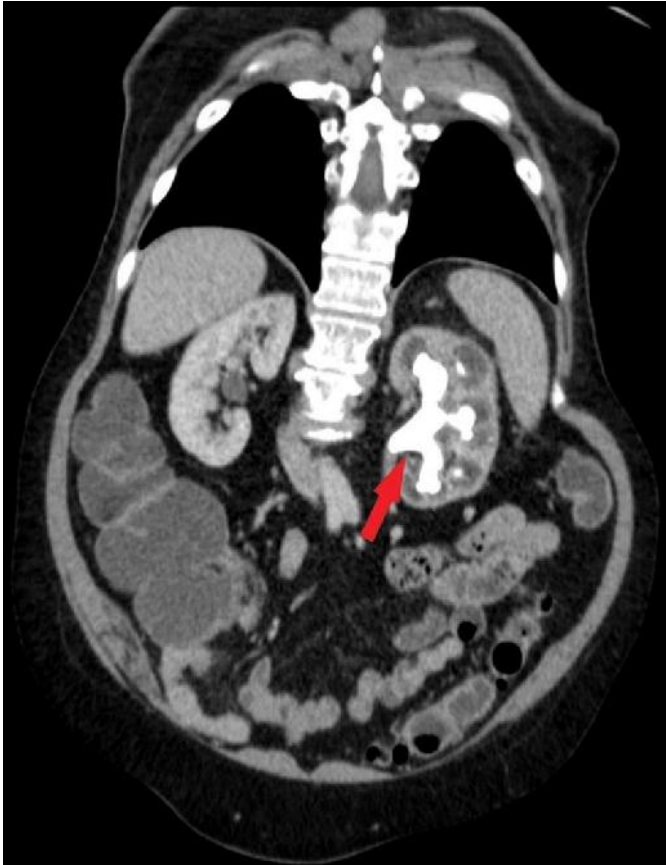


**FIGURE 17: Coronal oblique contrast-enhanced CT (CECT) during the nephrographic phase illustrates a complete staghorn calculus, which is prominently tapering the upper collecting system.**

This figure is the original work of the authors. Patient consent for the use of the image was obtained, as mentioned in the patient consent form (point no. 12).

---

### **Inflammation and inflammatory pathologies**

In severe or chronic pyelonephritis, renal inflammatory diseases often spread to the renal sinus and surrounding territory. Primary inflammatory lesions are rare. Renal sinus inflammation can resemble a tumor [25].

Due to recurrent urinary tract infections, usually caused by *Corynebacterium urealyticum*, calcifications in the pelvicalyceal system and ureter create encrusted uretero-pyelitis (Figure 18), an uncommon and severe condition. Calcium deposits on CT images aid diagnosis.



**FIGURE 18: Non-enhanced CT (NECT) scan (a), a contrast-enhanced CT**

**(CECT) scan in the nephrographic phase (b), and a urographic phase (c). The NECT scan (a) reveals wall calcifications within the pelvicalyceal systems and proximal ureters, as denoted by the arrowheads. Subsequent imaging with CECT during the nephrographic phase (b) provides enhanced visualization of the inflammatory changes within the pelvicalyceal systems and proximal ureters. Collectively, these imaging findings support the diagnosis of encrusted ureteropyelitis. There are also multiple calculi showcased during the excretory phase CECT.**

This figure is a republished image, permission was obtained from the original publisher, <https://epos.myesr.org/poster/esr/ecr2018/C-2802>

---

## **Miscellaneous pathologies**

### *Metal Toxicity*

The detection of metal objects in an imaging scan can cause severe, streak-like distortions (Figure 19). These occur because the metal has a density that exceeds the computer's capacity to handle, resulting in an inadequate reduction of image intensity.



**FIGURE 19: Non-enhanced CT (NECT) scans in the axial plane (a and b) depict a person who has been poisoned by heavy metals, exhibiting characteristic metallic artifacts on both sides. Heavy metals such as lead, mercury, arsenic, and cadmium can accumulate within the body tissues, including the bones and organs, leading to toxic effects. The metallic artifacts produce characteristic radiopaque shadows.**

This figure is a republished image, permission was obtained from the original publisher, <https://epos.myesr.org/poster/esr/ecr2018/C-2802>

---

## **Conclusions**

The renal sinus can have many pathological diseases, thus excretory urography, ultrasound, CT, MRI, and angiography are needed to diagnose

it quickly. Out of all the modalities, CT imaging with an IV contrast medium is essential for diagnosing and assessing renal sinus diseases. CT imaging helps characterize lesions and guide patient care by revealing their density and extent. With the help of CT imaging, we can characterize correctly the etiology of the plethora of pathologies that involve the renal sinus. Effective treatment requires knowledge of renal sinus pathology imaging and differential diagnosis.

### **Appendices**

Consents from patients for the use of the images were obtained, as mentioned in point no. 12 of the patient consent form (Figure 20).

**PATIENT CONSENT FORM**

1. Patient Name: \_\_\_\_\_  
 2. Date: \_\_\_\_\_  
 3. Signature: \_\_\_\_\_  
 4. Date: \_\_\_\_\_

5. Medical Record Number: \_\_\_\_\_

6. Doctor's Name: \_\_\_\_\_

7. Doctor's Signature: \_\_\_\_\_

8. Doctor's Title: \_\_\_\_\_

9. Doctor's Institution: \_\_\_\_\_

10. Doctor's Address: \_\_\_\_\_

11. Doctor's Phone: \_\_\_\_\_

12. Doctor's Fax: \_\_\_\_\_

13. Doctor's Email: \_\_\_\_\_

14. Doctor's Website: \_\_\_\_\_

15. Doctor's Social Media: \_\_\_\_\_

16. Doctor's LinkedIn: \_\_\_\_\_

17. Doctor's Facebook: \_\_\_\_\_

18. Doctor's Twitter: \_\_\_\_\_

19. Doctor's YouTube: \_\_\_\_\_

20. Doctor's Instagram: \_\_\_\_\_

21. Doctor's Snapchat: \_\_\_\_\_

22. Doctor's TikTok: \_\_\_\_\_

23. Doctor's Other: \_\_\_\_\_

24. Doctor's Other: \_\_\_\_\_

25. Doctor's Other: \_\_\_\_\_

26. Doctor's Other: \_\_\_\_\_

27. Doctor's Other: \_\_\_\_\_

28. Doctor's Other: \_\_\_\_\_

29. Doctor's Other: \_\_\_\_\_

30. Doctor's Other: \_\_\_\_\_

31. Doctor's Other: \_\_\_\_\_

32. Doctor's Other: \_\_\_\_\_

33. Doctor's Other: \_\_\_\_\_

34. Doctor's Other: \_\_\_\_\_

35. Doctor's Other: \_\_\_\_\_

36. Doctor's Other: \_\_\_\_\_

37. Doctor's Other: \_\_\_\_\_

38. Doctor's Other: \_\_\_\_\_

39. Doctor's Other: \_\_\_\_\_

40. Doctor's Other: \_\_\_\_\_

41. Doctor's Other: \_\_\_\_\_

42. Doctor's Other: \_\_\_\_\_

43. Doctor's Other: \_\_\_\_\_

44. Doctor's Other: \_\_\_\_\_

45. Doctor's Other: \_\_\_\_\_

46. Doctor's Other: \_\_\_\_\_

47. Doctor's Other: \_\_\_\_\_

48. Doctor's Other: \_\_\_\_\_

49. Doctor's Other: \_\_\_\_\_

50. Doctor's Other: \_\_\_\_\_

51. Doctor's Other: \_\_\_\_\_

52. Doctor's Other: \_\_\_\_\_

53. Doctor's Other: \_\_\_\_\_

54. Doctor's Other: \_\_\_\_\_

55. Doctor's Other: \_\_\_\_\_

56. Doctor's Other: \_\_\_\_\_

57. Doctor's Other: \_\_\_\_\_

58. Doctor's Other: \_\_\_\_\_

59. Doctor's Other: \_\_\_\_\_

60. Doctor's Other: \_\_\_\_\_

61. Doctor's Other: \_\_\_\_\_

62. Doctor's Other: \_\_\_\_\_

63. Doctor's Other: \_\_\_\_\_

64. Doctor's Other: \_\_\_\_\_

65. Doctor's Other: \_\_\_\_\_

66. Doctor's Other: \_\_\_\_\_

67. Doctor's Other: \_\_\_\_\_

68. Doctor's Other: \_\_\_\_\_

69. Doctor's Other: \_\_\_\_\_

70. Doctor's Other: \_\_\_\_\_

71. Doctor's Other: \_\_\_\_\_

72. Doctor's Other: \_\_\_\_\_

73. Doctor's Other: \_\_\_\_\_

74. Doctor's Other: \_\_\_\_\_

75. Doctor's Other: \_\_\_\_\_

76. Doctor's Other: \_\_\_\_\_

77. Doctor's Other: \_\_\_\_\_

78. Doctor's Other: \_\_\_\_\_

79. Doctor's Other: \_\_\_\_\_

80. Doctor's Other: \_\_\_\_\_

81. Doctor's Other: \_\_\_\_\_

82. Doctor's Other: \_\_\_\_\_

83. Doctor's Other: \_\_\_\_\_

84. Doctor's Other: \_\_\_\_\_

85. Doctor's Other: \_\_\_\_\_

86. Doctor's Other: \_\_\_\_\_

87. Doctor's Other: \_\_\_\_\_

88. Doctor's Other: \_\_\_\_\_

89. Doctor's Other: \_\_\_\_\_

90. Doctor's Other: \_\_\_\_\_

91. Doctor's Other: \_\_\_\_\_

92. Doctor's Other: \_\_\_\_\_

93. Doctor's Other: \_\_\_\_\_

94. Doctor's Other: \_\_\_\_\_

95. Doctor's Other: \_\_\_\_\_

96. Doctor's Other: \_\_\_\_\_

97. Doctor's Other: \_\_\_\_\_

98. Doctor's Other: \_\_\_\_\_

99. Doctor's Other: \_\_\_\_\_

100. Doctor's Other: \_\_\_\_\_

**FIGURE 20: Patient consent form**

**Additional Information**  
**Author Contributions**

All authors have reviewed the final version to be published and agreed to be accountable for all aspects of the work.

**Acquisition, analysis, or interpretation of data:** Loredana Sabina Cornelia Manolescu, Vlad-Octavian Bolocan, Georgian-Florentin

Diaconu, Mihaela Secareanu, Viorel Jinga, Maria-Glencora Costache, Gelu

Adrian Popa, Cosmin Medar

**Critical review of the manuscript for important intellectual content:**

Loredana Sabina Cornelia

Manolescu, Vlad-Octavian Bolocan, Viorel Jinga, Maria-Glencora Costache, Cosmin Medar

**Supervision:** Loredana Sabina Cornelia Manolescu, Vlad-Octavian Bolocan, Viorel Jinga, Maria-Glencora

Costache, Cosmin Medar

**Concept and design:** Vlad-Octavian Bolocan, Viorel Jinga, Maria-Glencora Costache, Cosmin Medar

**Drafting of the manuscript:** Vlad-Octavian Bolocan, Georgian-Florentin Diaconu, Mihaela Secareanu,

Viorel Jinga, Maria-Glencora Costache, Gelu Adrian Popa, Cosmin Medar

**Disclosures**

**Conflicts of interest:** In compliance with the ICMJE uniform disclosure form, all authors declare the following: **Payment/services info:** All authors have declared that no financial support was received from any organization for the submitted work. **Financial relationships:** All authors have declared that they have no financial relationships at present or within the previous three years with any organizations that might have an interest in the submitted work. **Other relationships:** All authors have declared that there are no other relationships or activities that could appear to have influenced the submitted work.

**Acknowledgements**

Maria-Glencora Costache has equal contribution with the first author.

**References**

1. [Rha SE, Byun JY, Jung SE, Oh SN, Choi YJ, Lee A, Lee JM: The renal sinus: pathologic spectrum and multimodality imaging approach. Radiographics. 2004, 24 Suppl 1:S117-31. 10.1148/rg.24si045503](#)
2. [Krishna S, Schieda N, Flood TA, Shanbhogue AK, Ramanathan S, Siegelman E: Magnetic resonance imaging \(MRI\) of the renal sinus. Abdom Radiol \(NY\). 2018, 43:3082-100. 10.1007/s00261-018-1593-1](#)

3. Kim JH, Park KJ, Kim MH, Kim JK: Preoperative assessment of renal sinus invasion by renal cell carcinoma according to tumor complexity and imaging features in patients undergoing radical nephrectomy. Korean J Radiol. 2021, 22:1323-31. [10.3348/kjr.2020.0984](https://doi.org/10.3348/kjr.2020.0984)
4. Gayer G, Zissin R: The renal sinus--transitional cell carcinoma and its mimickers on computed tomography . Semin Ultrasound CT MR. 2014, 35:308-19. [10.1053/j.sult.2014.02.004](https://doi.org/10.1053/j.sult.2014.02.004)
5. Sokhi HK, Mok WY, Patel U: Stage T3a renal cell carcinoma: staging accuracy of CT for sinus fat, perinephric fat or renal vein invasion. Br J Radiol. 2015, 88:20140504. [10.1259/bjr.20140504](https://doi.org/10.1259/bjr.20140504)
6. Silverman SG, Cohan RH: CT Urography: An Atlas. Lippincott Williams & Wilkins, Philadelphia, PA; 2007.
7. Rouprêt M, Seisen T, Birtle AJ, et al.: European Association of Urology guidelines on upper urinary tract urothelial carcinoma: 2023 update. Eur Urol. 2023, 84:49-64. [10.1016/j.eururo.2023.03.013](https://doi.org/10.1016/j.eururo.2023.03.013)
8. Bata P, Tarnoki DL, Tarnoki AD, et al.: Transitional cell and clear cell renal carcinoma: differentiation of distinct histological types with multiphase CT. Acta Radiol. 2014, 55:1112-9. [10.1177/0284185113510493](https://doi.org/10.1177/0284185113510493)
9. Kartal I, Uysal S, Adabag A, Gok A, Sagnak AL, Ersoy H: Aggressive squamous cell carcinoma of the renal pelvis. Niger J Clin Pract. 2019, 22:588-90. [10.4103/njcp.njcp\\_434\\_18](https://doi.org/10.4103/njcp.njcp_434_18)
10. Gu SQ, Yang L, Hu CH, Shang HL: Adenocarcinoma of the renal pelvis: Imaging findings and preliminary way of thinking in diagnosis. Asian J Surg. 2022, 45:1569-70. [10.1016/j.asjsur.2022.04.071](https://doi.org/10.1016/j.asjsur.2022.04.071)
11. Castillo RP, Santoscoy JF, Pisani L, Madrazo BL, Casillas VJ: Imaging of unusual renal tumors. Curr Urol Rep. 2019, 20:5. [10.1007/s11934-019-0867-7](https://doi.org/10.1007/s11934-019-0867-7)
12. Bokka S, Manikandan R, Dorairajan LN, Srivathsa K, Sreenivasan Sreerag K, Kalra S, Pottakat B: Perioperative and oncological outcomes of renal cell carcinoma with venous tumour thrombus . Urologia.

2022, 89:31-7. [10.1177/03915603211007030](https://doi.org/10.1177/03915603211007030)

13. [Granja MF, O'Brien AT, Trujillo S, Mancera J, Aguirre DA: Multilocular cystic nephroma: a systematic literature review of the radiologic and clinical findings. AJR Am J Roentgenol. 2015, 205:1188-93.](#)

[10.2214/AJR.15.14548](https://doi.org/10.2214/AJR.15.14548)

14. [Zhu Q, Zhu W, Wu J, Chen W: Imaging features of primary renal lymphoma . Acta Radiol. 2018, 59:114-20.](#)

[10.1177/0284185117706202](https://doi.org/10.1177/0284185117706202)

15. [Pinto F, Cappa E, Brescia A, et al.: Metastasis to the renal hilum from malignant melanoma of the anterior trunk: an unusual finding. Arch Ital Urol Androl. 2010, 82:119-21.](#)

16. [Fitzgerald E, Melamed J, Taneja SS, Rosenkrantz AB: MRI appearance of massive renal replacement lipomatosis in the absence of renal calculus disease. Br J Radiol. 2011, 84:e41-4. \[10.1259/bjr/42450182\]\(https://doi.org/10.1259/bjr/42450182\)](#)

17. [Sharma R, Khara S, Singh M, Sarangi SS, Begam I: Renal replacement lipomatosis: a rare and often ignored entity. Chonnam Med J. 2022, 58:81-2. \[10.4068/cmj.2022.58.2.81\]\(https://doi.org/10.4068/cmj.2022.58.2.81\)](#)

18. [Nicolau C, Antunes N, Paño B, Sebastia C: Imaging characterization of renal masses. Medicina \(Kaunas\). 2021, 57:51. \[10.3390/medicina57010051\]\(https://doi.org/10.3390/medicina57010051\)](#)

[10.3390/medicina57010051](https://doi.org/10.3390/medicina57010051)

19. [Koratala A, Alquadan KF: Parapelvic cysts mimicking hydronephrosis. Clin Case Rep. 2018, 6:760-1. \[10.1002/ccr3.1431\]\(https://doi.org/10.1002/ccr3.1431\)](#)

[10.1002/ccr3.1431](https://doi.org/10.1002/ccr3.1431)

20. [Kanchanasuttirak W, Claimon T, Kanchanasuttirak P: Idiopathic renal arteriovenous malformation: a case report. Asian J Surg. 2022, 45:2068-9. \[10.1016/j.asjsur.2022.04.099\]\(https://doi.org/10.1016/j.asjsur.2022.04.099\)](#)

21. [Hevia V, Gómez V, Hevia M, et al.: Troubleshooting complex vascular cases in the kidney graft: multiple vessels, aneurysms, and injuries during harvesting procedures. Curr Urol Rep. 2020, 21:5. \[10.1007/s11934-020-0955-8\]\(https://doi.org/10.1007/s11934-020-0955-8\)](#)

[10.1007/s11934-020-0955-8](https://doi.org/10.1007/s11934-020-0955-8)

22. [Kothari K, Hines JJ: CT imaging of emergent renal conditions . Semin Ultrasound CT MR. 2018, 39:129-44. \[10.1053/j.sult.2017.11.003\]\(https://doi.org/10.1053/j.sult.2017.11.003\)](#)

[10.1053/j.sult.2017.11.003](https://doi.org/10.1053/j.sult.2017.11.003)

- <sup>23.</sup> Gross JA, Lehnert BE, Linnau KF, Voelzke BB, Sandstrom CK: Imaging of urinary system trauma. Radiol Clin North Am. 2015, 53:773-88, ix. [10.1016/j.rcl.2015.02.005](https://doi.org/10.1016/j.rcl.2015.02.005)
- <sup>24.</sup> Wagner CA: Etiopathogenic factors of urolithiasis. Arch Esp Urol. 2021, 74:16-23.
- <sup>25.</sup> Papadopoulos GI, Mountanos IG, Manolakakis SI, Chrysanthakopoulos G, Papaliodi E, Farmakis AD: Chronic pyelonephritis presenting as a renal sinus tumor with retroperitoneal extension: a case report. J Med Case Rep. 2009, 3:9054. [10.4076/1752-1947-3-9054](https://doi.org/10.4076/1752-1947-3-9054)

## ANEXA 4

**Review began** 07/20/2024

**Review ended** 07/27/2024

**Published** 07/31/2024

© **Copyright** 2024

Bolocan et al. This is an open access article distributed under the terms of the Creative Commons Attribution License CC-BY 4.0., which permits unrestricted use, distribution, and reproduction in any medium, provided the original author and source are credited.

**DOI:** 10.7759/cureus.65880

**Open Access Case Report**

**Imaging Aspects in a Case of  
Persistent Müllerian**

**Duct Syndrome (PMDS): A Case Report and  
Overview**

1, 2 1 1 1

Vlad-Octavian Bolocan , Georgian-Florentin Diaconu , Alexandra Giuvelea , Mihaela Secareanu ,

1, 2 2 3 4, 5, 6

Cosmin Medar , Loredana S. Manolescu , Amelia Petrescu , Viorel Jinga

1. Department of Clinical Laboratory of Radiology and Medical Imaging, Clinical Hospital "Prof. Dr. Theodor Burghele",

Bucharest, ROU 2. Department of Fundamental Sciences, Faculty of Midwifery and Nursing, University of Medicine and

Pharmacy "Carol Davila", Bucharest, ROU 3. Department of Pathology, Clinical Hospital "Prof. Dr. Theodor Burghele", Bucharest, ROU 4.

Department of Urology, Clinical Hospital "Prof. Dr. Theodor Burghele", Bucharest, ROU 5.

Department of Urology, Faculty of Medicine, University of Medicine and Pharmacy "Carol Davila", Bucharest, ROU 6.

Medical Sciences Section, Academy of Romanian Scientists, Bucharest, ROU

**Corresponding author:** Cosmin Medar, [cosmin.medar@umfcd.ro](mailto:cosmin.medar@umfcd.ro)

---

---

### Abstract

Persistent Müllerian duct syndrome (PMDS) is a rare kind of internal male pseudohermaphroditism. The patient, who has a male karyotype and

phenotypic characteristics, exhibits Müllerian duct derivatives such as the uterus, cervix, fallopian tubes, and upper two-thirds of the vagina. This article provides a comprehensive analysis of the CT and MRI characteristics of a case of PMDS in a 35-year-old male patient who sought medical attention at our clinic due to pain in the left inguinal region and the presence of undescended testes on both sides. The imaging results showed a pelvic mass with a bicornuate appearance, situated adjacent to the bladder on the left side. The diagnosis of compensated hypergonadotropic hypogonadism with a normal male karyotype is confirmed through biological and genetic studies. The final diagnosis was confirmed through histopathological examination following laparoscopic transperitoneal surgical removal. The examination revealed a left lateral vesical pelvic tumor with a firm-elastic, bicornuate appearance, along with a thickened endometrium. Microscopic findings included simple glandular hyperplasia with edema in the endometrium, a small adenomatous polyp at the uterine fundus, and bilateral rigid cords consistent with vas deferens histology. The primary issue with PMDS is in its rarity, which consequently limits the availability of comprehensive case series and prospective research. As a result, radiologists and surgeons must possess knowledge of this ailment, as there is a scarcity of defined treatment guidelines and long-term care strategies.

---

**Categories:** Radiology

**Keywords:** müllerian duct, pseudohermaphroditism, management, uterus, male

### **Introduction**

Persistent Müllerian duct syndrome (PMDS) is a type of internal male pseudohermaphroditism (MPH) where the presence of the uterus and fallopian tubes indicates a failure in the sex differentiation pathway that relies on anti-Müllerian hormone (AMH) [1]. Consequently, these patients would have external genitalia and typical male traits, confirming the integrity of the androgen-dependent system. During imaging examinations for other problems or surgical correction of cryptorchidism or inguinal hernia, the Müllerian derivatives are typically detected inadvertently in PMDS. There have been two distinct anatomical forms that have been identified: In the typical scenario, one testis descends into the scrotum and pulls down the fallopian tube on the same side, as well as

the uterus, and subsequently the fallopian tube and testis on the opposite side. Occasionally, both testes might be found in an ovarian position, where they are located within the wide ligament. PMDS is a genetic disorder that occurs when there is a deficiency in the synthesis of AMH or when the target organs are resistant to AMH [2]. When dealing with Müllerian duct anomalies, it must be taken into consideration that these are often associated with other congenital malformations, such as renal agenesis [3].

### **Case Presentation**

A 35-year-old male patient, without any notable medical history, presented at our urological emergency room complaining of pain in the left groin area. The physical examination identified an underdeveloped left testicle, whereas the right testicle was not found in the right hemiscrotum.

The CT results showed a clearly defined mass in the pelvic region, situated superior to the bladder having "a uterine disposition" (Figure 1a, 1b, 1c). Even if morphologically descriptive, the body CT scan was unequivocal; therefore, a body MRI was performed, which confirmed Müllerian duct derivatives (i.e., uterus, cervix, and upper third of the vagina) in a close relationship with the prostate and the seminal vesicles. The sagittal T2-weighted image shows the normal anatomy of the uterus with three strata; however, the

**How to cite this article**  
Bolocan V, Diaconu G, Giuvelea A, et al. (July 31, 2024) Imaging Aspects in a Case of Persistent Müllerian Duct Syndrome (PMDS): A Case Report and Overview. *Cureus* 16(7): e65880. DOI 10.7759/cureus.65880  
endometrium drains in the prostatic urethra (Figure 2a, 2b). To further confirm the anatomy, the diffusionweighted imaging (DWI) and corresponding apparent diffusion coefficient (ADC) map showcase the increase in signal of the endometrium, which is validated on the axial T2 as a T2 "shine-through" artifact (Figure 3a, 3b, 3c).

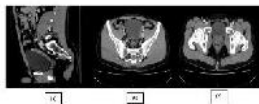


**FIGURE 1: Sagittal venous phase (a) and axial arterial phase (b) CT scans demonstrate a smooth contour, macronodular, with isoattenuation and minimally enhancing ovoidal mass arising from the pelvis, lateral and superior to the bladder. Axial arterial phase (c)**

**CT scan obtained lower demonstrates the presence and normal anatomy of the prostate gland.**

This figure is the original work of the authors. Patient consent for the use of the image was obtained, as mentioned in the patient consent form.

---

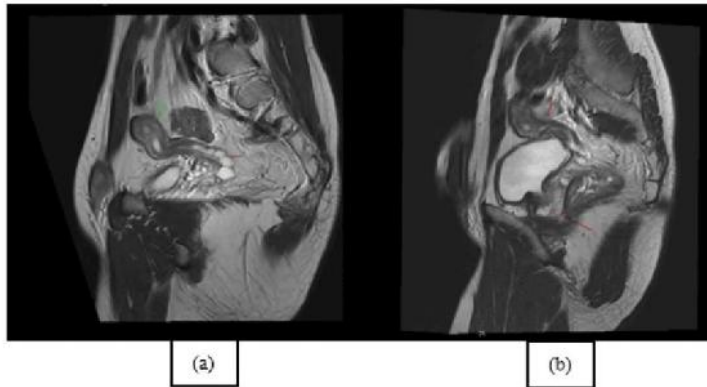


**FIGURE 2: Sagittal T2-weighted image (a) and sagittal oblique T2weighted image (b) show the zonal anatomy with the endometrium, which is hyperintense; the junctional zone as a hypointense band; and the outer myometrium with an intermediate signal. Also, on the sagittal T2-weighted image (a), there are also multiple cystic-like round nodules compatible with seminal vesicles; the sagittal oblique T2-weighted image (b) demonstrates the normal prostate anatomy shown before on CT scans.**

This figure is the original work of the authors. Patient consent for the use of the image was obtained, as mentioned in the patient consent form.

---

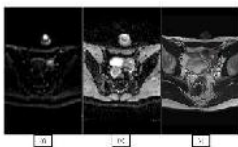


**FIGURE 3: Trace (a) and ADC (b) images show a signal increase in the center of the uterine structure; the axial T2 (c) confirms the T2 shinethrough artifact compatible with the endometrium.**

ADC: apparent diffusion coefficient

This figure is the original work of the authors. Patient consent for the use of the image was obtained, as mentioned in the patient consent form.

---

Additionally, there was an oval-shaped mass in the upper portion of the left inguinal canal, which could not be definitively identified on the body CT scan, leading to suspicion of a Müllerian vestige (Figure 4a, 4b).

Again, the MRI was diagnostic both with the coronal T2 (Figure 5) showcasing the heterogeneous mass and also with the follow-up sequences.

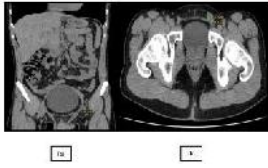


**FIGURE 4: Coronal and axial NECT scans of the pelvis show a small round, isoattenuating mass in the upper part of the left inguinal canal.**

NECT: non-contrast-enhanced computed tomography

This figure is the original work of the authors. Patient consent for the use of the image was obtained, as mentioned in the patient consent form.



**FIGURE 5: Coronal T2-weighted image MRI scan of the pelvis shows a small heterogeneous mass, with iso- and high T2 signal which raised the suspicion of hypoplastic testicle against Müllerian duct derivatives (further described below).**

This figure is the original work of the authors. Patient consent for the use of the image was obtained, as mentioned in the patient consent form.

---

Coronal T1-weighted images showcase the undescended testes and the spermatic cord. Furthermore, high signals on the DWI and on the T2FS confirm the diagnosis of cryptorchidism (Figure 6a, 6b, 6c).

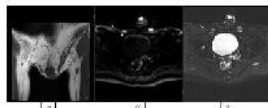


**FIGURE 6: Coronal T1-weighted image (a), trace image (b), and T2FS (c) confirm the diagnosis of cryptorchidism with typical T1 appearance of the undescended testes and the spermatic cord; the high signal on the trace image is fully diagnostic of the testes.**

This figure is the original work of the authors. Patient consent for the use of the image was obtained, as mentioned in the patient consent form.

---

Based on the laboratory analyses, the diagnosis of compensated hypergonadotropic hypogonadism could be confirmed. The semen study indicated the absence of sperm, and the genetic examination indicated a normal chromosomal structure. After the cystoscopy, the urethra and prostatic lodge are shown to have a normal appearance. The decision has been made to proceed with the surgical intervention for the pelvic tumor. The pelvic tumor is removed with laparoscopic transperitoneal surgery. An elastic and triangular tumor growth measuring around 6/4/3 cm is observed. It has a bicornuate appearance, with one horn extending towards the left deep inguinal hole and the other towards the right deep inguinal hole.

Pathological analysis further revealed a pelvic tumor formation localized to the left lateral vesical region, with a triangular shape measuring 6/4/3 cm, exhibiting a firm-elastic consistency and a bicornuate (uterinelike) appearance. On sectioning, a cavitory appearance is noted with a thickened mucosa (endometrium). Bilaterally along the exterior of the uterus, rigid cords are observed. Microscopically (Figure 7), the uterine wall consists of muscle fibers, small vessels with thickened walls, and endometrium exhibiting simple glandular hyperplasia and edema. Additionally, a small adenomatous polyp is present at the uterine fundus. On either side of the uterus, structures composed of concentric muscle fibers and connective tissue are observed, with a central papillary glandular appearance and the presence of pigment structures compatible with the histological composition of the vas deferens.

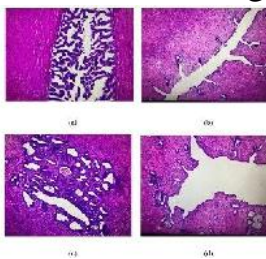


**FIGURE 7: Several microscopic images taken with a 4× objective lens and stained with H&E during the histopathological examination: (a) deferent duct, (b) uterus with endometrial focus, (c) uterus at a different level of sectioning with the endometrium and several grouped glands, some with a dilated appearance, and (d) uterus with slightly dilated uterine cavity and endometrium with a few glands.**

H&E: hematoxylin and eosin

This figure is the original work of the authors. Patient consent for the use of the image was obtained, as mentioned in the patient consent form.

---

The postoperative evolution was favorable, and the patient was discharged with a good general condition, afebrile, undergoing surgical healing. Regrettably, we lost the patient at follow-up as there were no further visits.

### **Discussion**

A rare form of MPH that is defined by the presence of the uterus, fallopian tubes, and upper part of the vagina in an otherwise normally differentiated 46,XY male is known as PMDS. The syndrome can be attributed to either an inadequate quantity of AMH or an insensitivity of the organ that is the target of the disease to this particular risk factor. Because it is a rare disorder, there are just a few case series that are very small, and there are no prospective studies that can provide clear guidance regarding treatment or longterm management [4-12].

In the published research, there are approximately 200 cases that have been reported. It is typically found in people who are being evaluated for infertility or cryptorchidism or while they are undergoing surgery that is performed on the abdominal region [13,14]. Regarding our situation, the results of the physical examination showed that the patient possesses a typical pattern of external genitalia. In spite of this, the patient was diagnosed with bilateral cryptorchidism and hypoplastic scrotum symptoms. Following the completion of the chromosomal investigation, it was discovered that the male karyotype known as 46,XY was seemingly normal, with no numerical or structural abnormalities.

Despite the fact that some of the individuals had normal spermatogenesis, infertility was a consequence of PMDS that was cited rather frequently. In the case that we examined, it was found that the patient had secondary infertility. When compared to patients who have an isolated undescended testis, patients who have PMDS have a significantly increased risk of acquiring testicular cancer. A total of 20 cases of PMDS with testicular cancer have been reported up to this point [15].

Seminoma is the most rare form of testicular cancer, followed by embryonal carcinoma, teratocarcinoma, and choriocarcinoma. Seminoma is the most common type of testicular cancer. On the other hand, there are findings that indicate that the incidence of Müllerian cancer is significantly lower than that of testicular cancer. Farikullah et al. have

reported a significant number of cases of malignant transformation of Müllerian derivatives in patients with PMDS. The rate of malignant transformation ranged from 3.1% to 8.4% [16,17].

In the treatment of patients with PMDS, the primary objectives are to control the undescended testes and Müllerian duct derivatives, to prevent the development of cancer from Müllerian remnants, and to safeguard the patient's fertility.

One of the most notable aspects of our case is the patient's age, as the majority of diagnoses connected with this ailment are made during childhood.

### **Conclusions**

This paper aims to highlight a unique instance of PMDS and provide a comprehensive review of the existing literature. PMDS should be considered as a potential diagnosis for patients who have either one or both testicles that have not descended. The diagnosis mostly relies on clinical, radiological, or intraoperative findings. The management should focus on eliminating the harmful characteristics of this entity and ensuring the preservation of the patient's ability to reproduce. Surgical removal of the Müllerian duct remnant is recommended.

The primary responsibility of the radiologist is not to identify a specific diagnosis but rather to precisely illustrate the structure of the genitourinary tract and the impact of the ailment on adjacent organs.

### **Additional Information**

#### **Author Contributions**

All authors have reviewed the final version to be published and agreed to be accountable for all aspects of the work.

**Concept and design:** Loredana S. Manolescu, Vlad-Octavian Bolocan, Georgian-Florentin Diaconu, Mihaela Secareanu, Cosmin Medar, Viorel Jinga, Alexandra Giuvelea, Amelia Petrescu

**Acquisition, analysis, or interpretation of data:** Loredana S. Manolescu, Vlad-Octavian Bolocan, Georgian-Florentin Diaconu, Mihaela Secareanu, Cosmin Medar, Viorel Jinga, Alexandra Giuvelea, Amelia Petrescu

**Drafting of the manuscript:** Loredana S. Manolescu, Vlad-Octavian Bolocan, Georgian-Florentin

Diaconu, Mihaela Secareanu, Cosmin Medar, Viorel Jinga, Alexandra Giuvelea, Amelia Petrescu

**Critical review of the manuscript for important intellectual content:**

Loredana S. Manolescu, Vlad-

Octavian Bolocan, Georgian-Florentin Diaconu, Mihaela Secareanu, Cosmin Medar, Viorel Jinga, Alexandra

Giuvelea, Amelia Petrescu

**Supervision:** Loredana S. Manolescu, Vlad-Octavian Bolocan, Georgian-Florentin Diaconu, Mihaela

Secareanu, Cosmin Medar, Viorel Jinga, Alexandra Giuvelea, Amelia Petrescu

### **Disclosures**

**Human subjects:** Consent was obtained or waived by all participants in this study. Ethics Committee of Clinical Hospital "Prof. Dr. Theodor Burghel" issued approval 2/2021. **Conflicts of interest:** In compliance

with the ICMJE uniform disclosure form, all authors declare the following: **Payment/services info:** All authors have declared that no

financial support was received from any organization for the submitted work. **Financial relationships:** All authors have declared that they have

no financial relationships at present or within the previous three years with any organizations that might have an interest in the submitted work.

**Other relationships:** All authors have declared that there are no other relationships or activities that could appear to have influenced the

submitted work.

### **Acknowledgements**

Publication of this paper was supported by the University of Medicine and Pharmacy "Carol Davila", through the institutional program Publish not Perish.

### **References**

1. Renu D, Rao BG, Ranganath K, Namitha: [Persistent Mullerian duct syndrome](#). Indian J Radiol Imaging. 2010, 20:72-4. [10.4103/0971-3026.59761](#)

2. Rey R, Picard JY: [Anti-Müllerian hormone](#). Encyclopedia of Hormones. Henry HL, Norman AW (ed):

Academic Press, Cambridge (MA); 2003. 146-53. [10.1016/B0-12-341103-3/00021-8](https://doi.org/10.1016/B0-12-341103-3/00021-8)

3. Foster BR, Fananapazir G: [Diagnostic imaging: genitourinary](#). Elsevier, Amsterdam, Netherlands; 2021.

4. [Koren AT, Lautin EM, Kutcher R, Rozenblit A, Banerjee TD: Testicular feminization: radiologic considerations in a unique form of cryptorchidism. Abdom Imaging. 1996, 21:272-4.](#)

[10.1007/s002619900063](https://doi.org/10.1007/s002619900063)

5. [Chavhan GB, Parra DA, Oudjhane K, Miller SF, Babyn PS, Pippi Salle FL: Imaging of ambiguous genitalia: classification and diagnostic approach. Radiographics. 2008, 28:1891-904. 10.1148/rg.287085034](#)

6. Semelka RC: [Abdominal-pelvic MRI](#). Wiley-Blackwell, Hoboken (NJ); 2010.

7. [Yalinkaya A, Yayla M, Erdemoglu M: Prenatal diagnosis of a fetus with androgen insensitivity syndrome \(AIS\). Prenat Diagn. 2007, 27:856-7. 10.1002/pd.1747](#)

8. [Bonilla-Musoles F, Kushner-Dávalos L, Raga F, Machado LE, Osborne NG: Androgen insensitivity syndrome: in utero diagnosis by four-dimensional sonography and amniotic fluid karyotype. J Clin Ultrasound. 2006, 34:30-2. 10.1002/jcu.20183](#)

9. Bluth E, Benson C: [Ultrasound: a practical approach to clinical problems](#). Thieme, New York (NY); 2007.

10. [Nezzo M, De Visschere P, T'sjoen G, Weyers S, Villeirs G: Role of imaging in the diagnosis and management of complete androgen insensitivity syndrome in adults. Case Rep Radiol. 2013, 2013:158484.](#)

[10.1155/2013/158484](https://doi.org/10.1155/2013/158484)

11. Tank J, Knoll A, Gilet A, Kim S: [Imaging characteristics of androgen insensitivity syndrome. Clin Imaging. 2015, 39:707-10. 10.1016/j.clinimag.2015.02.002](#)

[10.1016/j.clinimag.2015.02.002](https://doi.org/10.1016/j.clinimag.2015.02.002)

12. [Khan S, Mannel L, Koopman CL, Chimpiri R, Hansen KR, Craig LB: The use of MRI in the pre-surgical evaluation](#)

of patients with androgen insensitivity syndrome. J Pediatr Adolesc Gynecol. 2014, 27:e17-20.

10.1016/j.jpag.2013.05.006

13. Shinmura Y, Yokoi T, Tsutsui Y: A case of clear cell adenocarcinoma of the Müllerian duct in persistent Müllerian duct syndrome: the first reported case. Am J Surg Pathol. 2002, 26:1231-4. 10.1097/00000478-

200209000-00014

14. Wu HC, Chen JH, Lu HF, Shen WC: Persistent Müllerian duct syndrome with seminoma: CT findings . AJR Am J Roentgenol. 2000, 174:102-4. 10.2214/ajr.174.1.1740102

15. Alanazi AB, Aldhowayan A, Almuhanna MM, Alghamdi AM: Persistent Mullerian duct syndrome (PMDS): case report and review of literature. Urol Case Rep. 2022, 42:102031. 10.1016/j.eucr.2022.102031

16. Al-Asmar A, Abu-Qamar A, Al-Saidah N, Al-Kaabneh A, Al-Qaralleh A, Al-Hiari A: Persistant Mullerian duct syndrome with intra-abdominal seminoma. Urol Case Rep. 2020, 33:101342. 10.1016/j.eucr.2020.101342

17. Ahadi M, Soleimantabar H, Javanmard B, Zahedifard S: A rare case of persistent Mullerian duct syndrome and review of literature. Int J Cancer Manag. 2020, 13:e99102. 10.5812/ijcm.99102